

# Multiscale modelling couples patches of two-layer thin fluid flow

Meng Cao\*      A. J. Roberts†

September 19, 2021

## Abstract

The multiscale gap-tooth scheme uses a given microscale simulator of complicated physical processes to enable macroscale simulations by computing only small sparse patches. This article develops the gap-tooth scheme to the case of nonlinear microscale simulations of thin fluid flow. The microscale simulator is derived by artificially assuming the fluid film flow having two artificial layers but no distinguishing physical feature. Centre manifold theory assures that there exists a slow manifold in the two-layer fluid film flow. Eigenvalue analysis confirms the stability of the microscale simulator. This article uses the gap-tooth scheme to simulate the two-layer fluid film flow. Coupling conditions are developed by approximating the values at the edges of patches by neighbouring macroscale values. Numerical eigenvalue analysis suggests that the gap-tooth scheme with the developed two-layer microscale simulator empowers feasible computation of large scale simulations of fluid film flows. We also implement numerical simulations of the fluid film flow by the gap-tooth scheme. Comparison between a gap-tooth simulation and a microscale simulation over the whole domain demonstrates that the gap-tooth scheme feasibly computes fluid film flow dynamics with computational savings.

## Contents

### 1 Introduction

**2**

---

\*School of Mathematical Sciences, University of Adelaide, South Australia 5005. <mailto:meng.cao@adelaide.edu.au> or <mailto:mengcao1188216@gmail.com>

†School of Mathematical Sciences, University of Adelaide, South Australia 5005. <mailto:anthony.roberts@adelaide.edu.au>

<b>2</b>	<b>Construct the two-layer microscale simulator</b>	<b>4</b>
2.1	Governing equations and boundary conditions for two layer thin film flow . . . . .	4
2.2	Embed to support with centre manifold theory . . . . .	6
2.3	A low order model of the two layer flow . . . . .	7
2.4	Eigenanalysis of the microscale model . . . . .	11
<b>3</b>	<b>Gap-tooth simulation of the two layer thin fluid flow</b>	<b>16</b>
3.1	Coupling conditions on the odd patches . . . . .	17
3.2	Coupling conditions on the even patches . . . . .	18
3.3	The low order model of one layer flow . . . . .	20
<b>4</b>	<b>Numerical gap-tooth simulations of the two layer thin fluid flow</b>	<b>22</b>
<b>5</b>	<b>Conclusion</b>	<b>24</b>
<b>A</b>	<b>Ancillary computer algebra program</b>	<b>30</b>

# 1 Introduction

Mathematical equations describing geophysical fluid dynamics are typically written at the macroscale of kilometres. But the underlying turbulent flow and physics is best understood at the very much finer ‘microscale’ sub-metre scale. We aim to empower scientists and engineers to use brief bursts of a given microscale simulator of wave-like dynamics on small patches of the space-time domain in order to make efficient and accurate macroscale simulations without ever knowing a macroscale closure.

Our modelling further develops the equation-free gap-tooth scheme (Gear et al. 2003, Samaey, Kevrekidis & Roose 2005, Samaey, Roose & Kevrekidis 2005, Samaey et al. 2009, e.g.) to empower novel simulation of wave-like systems over large time and space scales from a *given* microscopic simulator. Previously most multiscale modelling techniques have been developed for dissipative systems (E & Engquist 2003, Kevrekidis et al. 2003, Roberts & Kevrekidis 2005, Hou et al. 2008, e.g.). We suppose that the wave-like microscale simulator is computationally expensive so that only small time and spatial domain simulations are feasible: one example of future interest is direct numerical simulation of depth resolved turbulent fluid floods. The aim is for the microscale simulator to provide the necessary data for the macroscopic computation, so that whenever the microscale simulator improves, then the overall macroscale simulation will correspondingly improve.

Cao & Roberts (2013) initiated the application of the gap-tooth scheme to linear wave equations with weak dissipation. Cao & Roberts (2014) then developed and theoretically supported the gap-tooth method for more general dispersive and

nonlinear wave-like systems, and as an indicative application and test, applied the methodology to a Smagorinski model of turbulent shallow water flow. The generic key is to use polynomial interpolation of macroscale quantities, across the unsimulated gap between patches, to provide coupling conditions on macroscale quantities on the edges of each patch of the microsimulator. However, in most applications the microscale simulator will have many internal modes. When there are such internal modes in the gap-tooth simulation, an outstanding issue is that at each time step we need to ‘lift’ the macroscale coupling data to an appropriate microscale configuration. As a first attempt to address this issue of lifting for wave-like dynamics, this paper uses the gap-tooth scheme to model viscous flow of a layer of fluid at moderate Reynolds number.

The flow of rainwater on the road, windscreen or other draining problems (Chang 1987, 1994*a*, e.g.), and paint and coating flows (Weinstein & Ruschak 2004, e.g.) are a few examples of fluid film flows. Dynamics of such thin film flows have been studied extensively (Benjamin 1957, Roberts 1997, 1998, Roy et al. 2002, e.g.). The first aim of this article is to construct a two-layer model for such thin film flow as the microscale simulator. The main reason to develop a two-layer model (Section 2) is that it has microscale modes requiring lifting, but without the full complexity of fully resolved vertical structures. However, the two-layer model is itself a novel model for fluid flows at moderate Reynolds number.

Consider a thin fluid flow of depth  $h(x, t)$  on an inclined plate with the slope  $\tan \theta$ . Section 2 artificially assumes two layers in the thin fluid flow, which have no distinguishing physical feature, as shown in Figure 1. From the Navier–Stokes PDEs and the boundary conditions on the free surface and the flat substrate, Section 2.2 uses centre manifold theory (Roberts 1988, 2013, Aulbach & Wanner 2000, Potzsche & Rasmussen 2006, e.g.) to derive a semi-slow two-layer model in the flow fields of depth  $h(x, t)$  and layer mean velocities  $\bar{u}_1(x, t)$  in the lower layer and  $\bar{u}_2(x, t)$  in the upper layer: nondimensionally the main parts of the model are

$$\frac{\partial h}{\partial t} = -\frac{1}{2} \left( \frac{\partial h \bar{u}_1}{\partial x} + \frac{\partial h \bar{u}_2}{\partial x} \right), \quad (1a)$$

$$\frac{\partial \bar{u}_1}{\partial t} \approx 0.826 \left( \tan \theta - \frac{\partial h}{\partial x} \right) + \frac{1}{\text{Re}} \left( -19.3 \frac{\bar{u}_1}{h^2} + 6.98 \frac{\bar{u}_2}{h^2} \right) - 1.48 \bar{u}_1 \frac{\partial \bar{u}_1}{\partial x}, \quad (1b)$$

$$\frac{\partial \bar{u}_2}{\partial t} \approx 1.002 \left( \tan \theta - \frac{\partial h}{\partial x} \right) + \frac{1}{\text{Re}} \left( 6.98 \frac{\bar{u}_1}{h^2} - 5.36 \frac{\bar{u}_2}{h^2} \right) - 1.25 \bar{u}_1 \frac{\partial \bar{u}_1}{\partial x}, \quad (1c)$$

for Reynolds number  $\text{Re}$ , and the plate slope  $\tan \theta$ . The right-hand sides of (1), and the more refined version (17), include the effects of gravitational forcing, bed drag, nonlinear advection, and dispersion.

The stability analysis in section 2.4 shows instabilities at high wavenumber: consequently, section 2.4 introduces an asymptotically consistent regularising operator to stabilise the two-layer model.

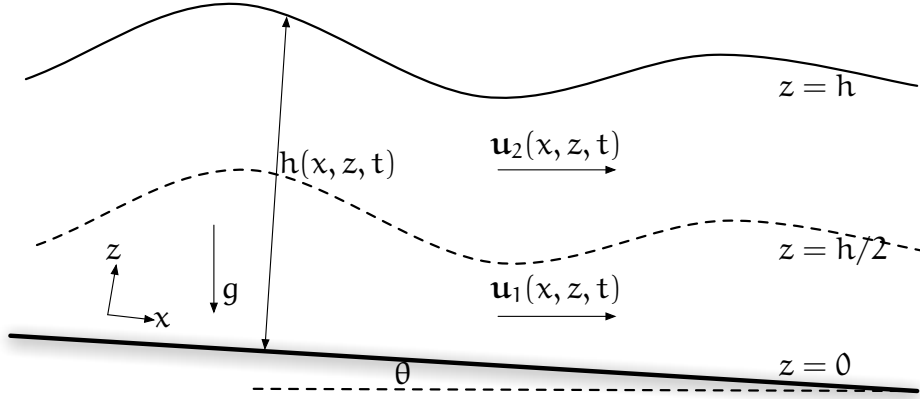


Figure 1: Diagram of the two-layer modelling of thin film flow. Assume the fluid film flow has two artificial layers, which have no distinguishing physical feature. Each layer has thickness  $h(x, t)/2$  and a mean layer velocity  $u_j(x, z, t)$  with  $j = 1$  for lower layer and  $j = 2$  for upper layer. The plate has a slope  $\tan \theta$ . Then  $x$  and  $z$  are the lateral and normal coordinates, and  $g$  is gravity.

Section 3 applies the gap-tooth scheme to simulate the fluid film flow with the two-layer model being the microscale simulator. The coupling conditions are extended by the novel proposed lifting of the one-layer mean velocity  $\bar{u}(x, t)$  to the two-layer velocities  $\bar{u}_1(x, t)$  and  $\bar{u}_2(x, t)$ . Comparisons between the gap-tooth simulation and the microscale simulation over the whole domain, Section 4, indicate that the gap-tooth scheme successfully simulates the dynamics of thin fluid flow at moderate Reynolds numbers.

## 2 Construct the two-layer microscale simulator

This section describes the derivation of the two-layer model. First, section 2.1 lists the 2D continuity and Navier–Stokes equations of a layer thin fluid flow and the boundary conditions on the free surface and on the plate. Second, section 2.2 embeds these equations in a family of equations with modified surface stress and mid-depth continuity so that an emergent two-layer slow manifold exists. The computer algebra of Appendix A then constructs the two-layer manifold model as summarised in section 2.3.

### 2.1 Governing equations and boundary conditions for two layer thin film flow

Consider a thin fluid flow of depth  $h(x, t)$  flowing down an inclined plate with slope  $\tan \theta$ . Denote the coordinate system by  $x$  and  $z$  along and normal to the plate.

Assume the fluid film flow has two artificial layers, each of thickness  $h(x, t)/2$ , which have no distinguishing physical feature, as shown schematically in Figure 1. Each layer velocity field  $\mathbf{q}_j(x, z, t) = (\mathbf{u}_j, w_j)$  and pressure field by  $p_j(x, z, t)$ , where  $j = 1$  is for lower layer and  $j = 2$  is for upper layer.

We nondimensionalise the system in terms of a typical film thickness  $H$ , a typical fluid velocity  $\mathbf{U} := \sqrt{gH}$ , the constant density  $\rho$ , and the slope angle of the plate  $\theta$ . Then the Reynolds number  $Re = H\mathbf{U}/\nu_f$  with  $\nu_f$  being the viscosity of the fluid. The nondimensional continuity and Navier–Stokes equations for the dynamics of the 2D fluid film flow are then

$$\nabla \cdot \mathbf{q}_j = \frac{\partial u_j}{\partial x} + \frac{\partial w_j}{\partial z} = 0, \quad j = 1, 2, \quad (2)$$

$$\frac{\partial \mathbf{q}_j}{\partial t} + \mathbf{q}_j \cdot \nabla \mathbf{q}_j = -\nabla p_j + \frac{1}{Re} \nabla^2 \mathbf{q}_j + \mathbf{g}, \quad j = 1, 2, \quad (3)$$

where the Reynolds number  $Re$  characterises the importance of the inertial terms compared to viscous dissipation, and where the vector  $\mathbf{g} = (\tan \theta, -1)$  is the nondimensional forcing by gravity.

Well-known nondimensional boundary conditions hold on the plate and on the free surface.

- On the plate, prescribing no-slip requires

$$\mathbf{u}_1 = w_1 = 0 \quad \text{on } z = 0. \quad (4)$$

- On the free surface, the pressure is assumed to be zero and so the stress normal to the surface is zero for zero surface tension (Roberts 1997, 1998, e.g.):

$$2 \left[ \frac{\partial w_2}{\partial z} + \left( \frac{\partial h}{\partial x} \right)^2 \frac{\partial u_2}{\partial x} - \frac{\partial h}{\partial x} \left( \frac{\partial u_2}{\partial z} + \frac{\partial w_2}{\partial x} \right) \right] - Re \left[ 1 + \left( \frac{\partial h}{\partial x} \right)^2 \right] p_2 = 0 \quad \text{on } z = h, \quad (5)$$

- The free surface having zero tangential stress results in

$$\left[ 1 - \left( \frac{\partial h}{\partial x} \right)^2 \right] \left( \frac{\partial u_2}{\partial z} + \frac{\partial w_2}{\partial x} \right) + 2 \left( \frac{\partial h}{\partial x} \right) \left( \frac{\partial w_2}{\partial z} - \frac{\partial u_2}{\partial x} \right) = 0 \quad \text{on } z = h. \quad (6)$$

- Also on the free surface, the kinematic condition is

$$\frac{\partial h}{\partial t} = w_2 - u_2 \frac{\partial h}{\partial x} \quad \text{on } z = h. \quad (7)$$

- Lastly, on the artificial interface of the two artificial layers, continuity of the physical fields requires

$$p_1 = p_2 \quad \text{on } z = h/2, \quad (8)$$

$$\mathbf{u}_1 = \mathbf{u}_2 \quad \text{on } z = h/2, \quad (9)$$

$$w_1 = w_2 \quad \text{on } z = h/2, \quad (10)$$

$$\frac{\partial \mathbf{u}_1}{\partial z} = \frac{\partial \mathbf{u}_2}{\partial z} \quad \text{on } z = h/2. \quad (11)$$

The PDEs (2)–(3), together with the boundary conditions (4)–(11) describe the dynamics of fluid film flow on an inclined plate.

## 2.2 Embed to support with centre manifold theory

This section embeds the system of physical equations in a family of artificial problems parametrised by  $\gamma$ . This embedding empowers theoretical support for the two-layer model.

First modify the tangential stress surface condition (6) to have an artificial forcing proportional to the net shear in the upper layer velocity:

$$\begin{aligned} & \left[ 1 - \left( \frac{\partial h}{\partial x} \right)^2 \right] \left( \frac{\partial \mathbf{u}_2}{\partial z} + \frac{\partial w_2}{\partial x} \right) + 2 \left( \frac{\partial h}{\partial x} \right)^2 \left( \frac{\partial w_2}{\partial z} - \frac{\partial \mathbf{u}_2}{\partial x} \right) \\ & = (1 - \gamma) \frac{2}{h} [\mathbf{u}_2 - \mathbf{u}_2(x, h/2, t)] \quad \text{on } z = h. \end{aligned} \quad (12)$$

When evaluated at parameter  $\gamma = 1$ , the right-hand side of (12) vanishes and so this artificial boundary condition (12) reduces to the physical tangential stress conditions (6). Also modify the derivative continuity (11) on the interface of the two artificial layers to

$$\left( 1 - \frac{\gamma}{2} \right) \frac{\partial \mathbf{u}_1}{\partial z} = \frac{\gamma}{2} \frac{\partial \mathbf{u}_2}{\partial z} + 2(1 - \gamma) \frac{\mathbf{u}_1}{h} \quad \text{on } z = h/2. \quad (13)$$

When evaluated at  $\gamma = 1$ , this artificial interface condition (13) recovers the originally physical interface condition (11). These are the two modifications of the embedding.

The theoretical support is based upon a subspace of equilibria. In the absence of lateral variations,  $\partial_x = 0$ , for parameter  $\gamma = 0$ , and on a horizontal bed,  $\theta = 0$ , the fluid system (2)–(11) modified by equations (12) and (13) has two neutral modes of the layer shear flows  $(\mathbf{u}_1, \mathbf{u}_2) \propto (z, h/2)$  and  $(\mathbf{u}_1, \mathbf{u}_2) \propto (0, z - h/2)$ . Conservation of fluid provides a third neutral mode in the dynamics. That is, under the assumptions  $\gamma = \partial_x = \theta = 0$ , there are three neutral modes, and hence a three dimensional ‘slow’ subspace of equilibria, corresponding to uniform shear flows on

a fluid of any thickness  $h$ . In the state space  $(h, u_1, u_2, w_1, w_2, p_1, p_2)$  the slow subspace is

$$\mathbb{E}_0 = \text{span} \left\{ \begin{bmatrix} 1 \\ 0 \\ 0 \\ 0 \\ 0 \\ 0 \end{bmatrix}, \begin{bmatrix} 0 \\ z \\ h/2 \\ 0 \\ 0 \\ 0 \end{bmatrix}, \begin{bmatrix} 0 \\ 0 \\ z-h/2 \\ 0 \\ 0 \\ 0 \end{bmatrix} \right\}.$$

Linearised about any equilibrium in the slow subspace  $\mathbb{E}_0$  (together with the small parameters  $\gamma = \partial_x = \theta = 0$ ), equations (2), (4) and (10) imply the normal velocity components  $w_1 = w_2 = 0$ . Then in the linearised system the normal component of the linearised PDE (3) with (5) and (8) establishes the pressures  $p_1 = p_2 = 0$ . Linearising the lateral component of the linearised PDE (3) together with the modified boundary conditions (9) and (12)–(13) gives a linear system for the lateral velocities  $u_j$ :

$$\frac{\partial u_j}{\partial t} - \frac{1}{\text{Re}} \frac{\partial^2 u_j}{\partial z^2} = 0, \quad (14a)$$

$$u_1 - u_2 = 0 \quad \text{on} \quad z = h/2, \quad (14b)$$

$$\frac{\partial u_2}{\partial z} - \frac{2}{h} [u_2 - u_2|_{z=h/2}] = 0 \quad \text{on} \quad z = h, \quad (14c)$$

$$\frac{\partial u_1}{\partial z} - \frac{2}{h} u_1 = 0 \quad \text{on} \quad z = h/2. \quad (14d)$$

The linearised PDE (14a) implies the eigenvalue  $\lambda = -k^2/\text{Re}$  by seeking the eigenvector of the lateral velocities  $(u_1, u_2) \propto (0, \sin k(h-z))$ . The boundary condition (14c) imposes the constraint  $kh/2 = \tan kh/2$  with solutions  $kh = 0, 8.986, 15.451, \dots$ . There exist a corresponding linearly independent generalised eigenvector with lower lateral velocity  $u_1 \neq 0$ . A spectral gap exists between the three zero eigenvalues of the slow subspace  $\mathbb{E}_0$  and the non-zero eigenvalues headed by  $\lambda \approx -80.763/(h^2 \text{Re})$ .

Given the spectral gap, centre manifold theory for such ‘infinite dimensional’ systems (Roberts 1988, 2013, Aulbach & Wanner 2000, Potzsche & Rasmussen 2006, e.g.) supports the existence, emergence and construction of a slow manifold model based upon the slow subspace shear modes. The slow manifold is constructed as a regular perturbation of the slow subspace (Roberts 1988, Potzsche & Rasmussen 2006). Importantly, the theory supports the model in a finite domain of the parameters  $\gamma$ ,  $\theta$  and  $\partial_x$ . Evaluating the resulting slow manifold model at the physical case of artificial parameter  $\gamma = 1$  then provides the model for the physical flow dynamics. Table 1 [p.10] shows evidence that the modelling converges at  $\gamma = 1$ .

### 2.3 A low order model of the two layer flow

Computer algebra (Appendix A) constructs the semi-slow manifold of the two layer thin fluid flow: we call it ‘semi-slow’ because the model resolves two lateral shear

modes, and because we use ‘slow’ to refer to a model that resolves only the gravest lateral shear mode. The computer algebra program derives the semi-slow model in the flow fields of depth  $h(x, t)$ , lower layer mean velocity  $\bar{u}_1(x, t)$  and upper layer mean velocity  $\bar{u}_2(x, t)$ .

The order of errors in the construction is phrased in terms of small parameters. In the theoretical support, the subspace of equilibria are found for  $\theta = \partial_x = \gamma = 0$  and so these are necessarily small parameters of the semi-slow manifold. Small lateral spatial derivative  $\partial_x$  corresponds to physical solutions varying slowly in  $x$  and in such a context has recently been made a rigorous approximation (Roberts 2013). Because the theoretical support is based upon the 3D subspace of equilibria parametrised by  $h$ ,  $\bar{u}_1$  and  $\bar{u}_2$ , the semi-slow model is formally global in  $h$ ,  $\bar{u}_1$  and  $\bar{u}_2$ . Nonetheless, we typically discard high order terms in  $\bar{u}_j$  as being insignificant in practical parameter regimes (Roberts 1998, e.g.). Thus  $\mathcal{O}(\bar{u}_1^p + \bar{u}_2^p + \partial_x^p + \theta^p)$  denotes the error terms for some exponent  $p$ , which means each term explicitly expressed in the model has in total less than  $p$  factors of these four parameters. The bigger the exponent number  $p$ , the higher the order of the modelling. The artificial small parameter  $\gamma$  has no physical meaning but is crucial to rigorously establish the semi-slow manifold. However, relatively high orders of the artificial parameter  $\gamma$  are required so that evaluating at  $\gamma = 1$  is accurate.

Computer algebra in Appendix A derives the physical flow fields of pressures  $p_1$  and  $p_2$ , and layer velocities  $u_1$  and  $u_2$  in terms of the film thickness  $h$ , layer mean velocities  $\bar{u}_1$  and  $\bar{u}_2$ , and scaled local normal coordinate  $Z = z/h$ :

$$\begin{aligned}
p_1 &= (1 - Z)h \\
&+ h^2 \frac{\partial^2 h}{\partial x^2} [-0.422 + 0.104Z - 0.5Z^2] + \gamma(-0.0148 - 0.0107) \\
&+ h \tan \theta \frac{\partial h}{\partial x} [(0.0469 - 0.104Z) + \gamma(0.0375 + 0.0107Z)] \\
&+ \frac{2}{\text{Re}} \left[ \left( \frac{\partial \bar{u}_1}{\partial x} - \frac{\partial \bar{u}_2}{\partial x} - 2 \frac{\partial \bar{u}_1}{\partial x} Z \right) + \frac{1}{h} \frac{\partial h}{\partial x} (\bar{u}_1 + \bar{u}_2 - 2\bar{u}_1 Z) \right] \\
&+ \gamma \frac{1}{\text{Re}} \left[ (4.875 \frac{\partial \bar{u}_1}{\partial x} - 1.125 \frac{\partial \bar{u}_2}{\partial x} - 1.5 \frac{\partial \bar{u}_1}{\partial x} Z + 0.5 \frac{\partial \bar{u}_2}{\partial x} Z) \right. \\
&\left. + \frac{1}{h} \frac{\partial h}{\partial x} (-7.625\bar{u}_1 + 2.375\bar{u}_2 + 1.5\bar{u}_1 Z - 0.5\bar{u}_2 Z) \right] \\
&+ \mathcal{O}(\bar{u}_1^3 + \bar{u}_2^3 + \partial_x^3 + \theta^3, \gamma^2), \tag{15a} \\
p_2 &= (1 - Z)h \\
&+ h^2 \frac{\partial^2 h}{\partial x^2} [(-0.417 + 0.115Z - 0.5Z^2) + \gamma(-0.0178 - 0.0049Z)] \\
&+ h \tan \theta \frac{\partial h}{\partial x} [(0.0521 - 0.115Z) + \gamma(0.0404 + 0.0049Z)]
\end{aligned}$$



$$\begin{aligned}
& + \frac{4}{\text{Re}} \left[ \left( -\frac{\partial \bar{u}_1}{\partial x} - \frac{\partial \bar{u}_2}{\partial x} + 2 \frac{\partial \bar{u}_1}{\partial x} Z \right) + \frac{1}{h} \frac{\partial h}{\partial x} (2\bar{u}_1 - \bar{u}_2 - 2\bar{u}_1 Z + \bar{u}_2 Z) \right] \\
& + \gamma \frac{1}{\text{Re}} \left[ \left( 11 \frac{\partial \bar{u}_1}{\partial x} - 3 \frac{\partial \bar{u}_2}{\partial x} - 13.75 \frac{\partial \bar{u}_1}{\partial x} Z + 4.25 \frac{\partial \bar{u}_2}{\partial x} Z \right) \right. \\
& \left. + \frac{1}{h} \frac{\partial h}{\partial x} (-13.75 \bar{u}_1 + 4.25 \bar{u}_2 + 13.75 \bar{u}_1 Z - 4.25 \bar{u}_2 Z) \right] \\
& + \mathcal{O}(\bar{u}_1^3 + \bar{u}_2^3 + \partial_x^3 + \theta^3, \gamma^2), \tag{15b}
\end{aligned}$$

$$\begin{aligned}
\mathbf{u}_1(Z) = & [(4.0 + 1.5\gamma)\bar{u}_1 Z - 0.5\gamma\bar{u}_2 Z + (4.0\bar{u}_2 - 12.0\bar{u}_1)\gamma Z^3] \\
& + \text{Re } h^2 \frac{\partial h}{\partial x} [(-0.104 + 0.0107\gamma)Z + 0.5Z^2 \\
& - (0.5 + 0.123\gamma)Z^3 + 0.225\gamma Z^5] \\
& + \text{Re } h^2 \tan \theta [(0.104 - 0.0107\gamma)Z - 0.5Z^2 \\
& + (0.5 + 0.123\gamma)Z^3 - 0.225\gamma Z^5] \\
& + \mathcal{O}(\bar{u}_1^3 + \bar{u}_2^3 + \partial_x^3 + \theta^3, \gamma^2), \tag{15c}
\end{aligned}$$

$$\begin{aligned}
\mathbf{u}_2(Z) = & [(6.0 - 11.9\gamma)\bar{u}_1 + (-2.0 + 4.13\gamma)\bar{u}_2 + (4.0 - 17.8\gamma)\bar{u}_2 Z \\
& + (-8.0 + 48.3\gamma)\bar{u}_1 Z + (27.0\bar{u}_2 - 69.0\bar{u}_1)\gamma Z^2 \\
& + (34.0\bar{u}_1 - 14.0\bar{u}_2)\gamma Z^3] \\
& + \text{Re } h^2 \frac{\partial h}{\partial x} [(-0.089 + 0.10\gamma) + (0.45 - 0.68\gamma)Z \\
& + (-0.63 + 1.8\gamma)Z^2 + (0.25 - 2.5\gamma)Z^3 + 1.8\gamma Z^4 - 0.49\gamma Z^5] \\
& + \text{Re } h^2 \tan \theta [(0.089 - 0.10\gamma) + (-0.45 + 0.68\gamma)Z \\
& + (0.63 - 1.8\gamma)Z^2 + (-0.25 + 2.5\gamma)Z^3 - 1.8\gamma Z^4 + 0.49\gamma Z^5] \\
& + \mathcal{O}(\bar{u}_1^3 + \bar{u}_2^3 + \partial_x^3 + \theta^3, \gamma^2). \tag{15d}
\end{aligned}$$

Equations (15) describe the low order shape of the manifold in the state space. Physically, upon setting the parameter  $\gamma = 1$ , these four equations (15) approximately describe the vertical structures of the pressures and layer velocities associated with the terms of depth  $h(x, t)$ , layer mean velocities  $\bar{u}_j(x, t)$  and their lateral derivatives. One important feature of this approach is that we do not impose these vertical structures on the flow: instead we systematically solve the governing physical fluid equations to discover the structure functions appropriate for any suitable parameter regime.

The computer algebra in Appendix A also determines the evolutions of the depth  $h(x, y)$  and layer mean velocities  $\bar{u}_1(x, t)$  and  $\bar{u}_2(x, t)$  on this semi-slow manifold (15) but now to high order in the parameter  $\gamma$ :

$$\begin{aligned}
\frac{\partial h}{\partial t} & = -0.5 \frac{\partial}{\partial x} (h\bar{u}_1 + h\bar{u}_2), \tag{16a} \\
\frac{\partial \bar{u}_1}{\partial t} & = (0.75 + 0.0438\gamma + 0.0365\gamma^2 - 0.00439\gamma^3 + 0.0000522\gamma^4)
\end{aligned}$$

Table 1: Partial sums from evaluating coefficients at  $\gamma = 1$  of selected terms in equation (16b)–(16c) indicates that the power series in  $\gamma$  converges quickly.

	$\partial h/\partial x$ in (16b)	$\partial h/\partial x$ in (16c)	$\bar{u}_1/h^2/\text{Re}$ in (16b)	$\bar{u}_1/h^2/\text{Re}$ in (16c)	$\bar{u}_2/h^2/\text{Re}$ in (16b)	$\bar{u}_2/h^2/\text{Re}$ in (16c)
$\gamma^0$	−0.75	−1.125	0	0	0	0
$\gamma^1$	−0.7938	−0.930	−18.	15.	6.	−9.
$\gamma^2$	−0.8302	−1.004	−19.35	6.712	7.050	−5.288
$\gamma^3$	−0.8258	−1.002	−19.42	6.933	7.012	−5.333
$\gamma^4$	−0.8259	−1.002	−19.34	6.960	6.990	−5.350
$\gamma^5$	−0.8256	−1.002	−19.32	6.974	6.982	−5.356
$\gamma^6$	−0.8255	−1.002	−19.32	6.977	6.980	−5.357

$$\begin{aligned}
& -0.000305\gamma^5 - 0.0000393\gamma^6 \left( \tan \theta - \frac{\partial h}{\partial x} \right) \\
& + \frac{1}{\text{Re}} \left[ - (18\gamma + 1.35\gamma^2 + 0.0723\gamma^3 - 0.0869\gamma^4 - 0.0112\gamma^5 - 0.00637\gamma^6) \frac{\bar{u}_1}{h^2} \right. \\
& \left. + (6.0\gamma + 1.05\gamma^2 - 0.038\gamma^3 - 0.022\gamma^4 - 0.008\gamma^5 - 0.00218\gamma^6) \frac{\bar{u}_2}{h^2} \right] \\
& + \mathcal{O}(\bar{u}_1^3 + \bar{u}_2^3 + \partial_x^3 + \theta^3, \gamma^7), \tag{16b}
\end{aligned}$$

$$\begin{aligned}
\frac{\partial \bar{u}_2}{\partial t} &= (1.125 - 0.195\gamma + 0.0740\gamma^2 - 0.00126\gamma^3 - 0.0003062\gamma^4 \\
& - 0.000185\gamma^5 - 0.0000231\gamma^6) \left( \tan \theta - \frac{\partial h}{\partial x} \right) \\
& + \frac{1}{\text{Re}} \left[ (15\gamma - 8.29\gamma^2 + 0.22\gamma^3 + 0.0278\gamma^4 + 0.0135\gamma^5 + 0.00351\gamma^6) \frac{\bar{u}_1}{h^2} \right. \\
& \left. + (-9.0\gamma + 3.17\gamma^2 - 0.0456\gamma^3 - 0.0173\gamma^4 - 0.00559\gamma^5 - 0.00146\gamma^6) \frac{\bar{u}_2}{h^2} \right] \\
& + \mathcal{O}(\bar{u}_1^3 + \bar{u}_2^3 + \partial_x^3 + \theta^3, \gamma^7), \tag{16c}
\end{aligned}$$

Equation (16a) is a direct consequence of conservation of fluid. The momentum equations (16b)–(16c) include the effects of viscous drag and dissipation  $\bar{u}_j/h^2$ , and the gravity forcing  $\tan \theta - \partial h/\partial x$ . The higher order physical effects of advection and dispersion effects are included in the next equations (17b)–(17c) where we report on the model to errors  $\mathcal{O}(\bar{u}_1^4 + \bar{u}_2^4 + \partial_x^4 + \theta^4, \gamma^7)$ .

Equations (15a)–(16c) express the semi-slow manifold model in terms of the introduced artificial parameter  $\gamma$ . Every coefficient in these equations is a power series in  $\gamma$ . The partial sums in Table 1 indicate that these coefficient series in  $\gamma$  converges quickly for  $\gamma = 1$ . Thus, when the model is constructed to

errors  $\mathcal{O}(\gamma^7)$ , it is apparent that all the shown digits are accurate. Roberts (1997, 1998) and Roberts et al. (2002) reported similar convergence in other related physical problems. Hereafter we calculate every coefficient in the model up to errors  $\mathcal{O}(\gamma^7)$ , and then evaluate at the artificial parameter  $\gamma = 1$ .

Truncating to errors  $\mathcal{O}(\bar{u}_1^4 + \bar{u}_2^4 + \partial_x^4 + \theta^4, \gamma^7)$ , omitting the intricate details of the derivation and upon setting the artificial parameter  $\gamma = 1$ , the evolution of the depth  $h(x, t)$ , the lower layer mean velocity  $\bar{u}_1(x, t)$  and the upper layer mean velocity  $\bar{u}_2(x, t)$  on the semi-slow manifold are described by the flow conservation equation and by effective lateral momentum equations

$$\frac{\partial h}{\partial t} = -0.5 \left( \frac{\partial h \bar{u}_1}{\partial x} + \frac{\partial h \bar{u}_2}{\partial x} \right), \quad (17a)$$

$$\begin{aligned} \frac{\partial \bar{u}_1}{\partial t} \approx & 0.826 \left( \tan \theta - \frac{\partial h}{\partial x} \right) + \frac{1}{\text{Re}} \left( -19.3 \frac{\bar{u}_1}{h^2} + 6.98 \frac{\bar{u}_2}{h^2} \right) \\ & - 1.48 \bar{u}_1 \frac{\partial \bar{u}_1}{\partial x} - 0.225 \bar{u}_2 \frac{\partial \bar{u}_2}{\partial x} + 0.142 \bar{u}_2 \frac{\partial \bar{u}_1}{\partial x} + 0.0728 \bar{u}_1 \frac{\partial \bar{u}_2}{\partial x} \\ & + \frac{(\bar{u}_1 - \bar{u}_2)}{h} (-0.25 \bar{u}_1 + 0.34 \bar{u}_2) \frac{\partial h}{\partial x} \\ & + \frac{1}{\text{Re}} \left( -3.84 \frac{\partial^2 \bar{u}_1}{\partial x^2} + 2.52 \frac{\partial^2 \bar{u}_2}{\partial x^2} \right), \end{aligned} \quad (17b)$$

$$\begin{aligned} \frac{\partial \bar{u}_2}{\partial t} \approx & 1.002 \left( \tan \theta - \frac{\partial h}{\partial x} \right) + \frac{1}{\text{Re}} \left( 6.98 \frac{\bar{u}_1}{h^2} - 5.36 \frac{\bar{u}_2}{h^2} \right) \\ & - 1.25 \bar{u}_1 \frac{\partial \bar{u}_1}{\partial x} - 1.57 \bar{u}_2 \frac{\partial \bar{u}_2}{\partial x} + 0.768 \bar{u}_2 \frac{\partial \bar{u}_1}{\partial x} + 0.930 \bar{u}_1 \frac{\partial \bar{u}_2}{\partial x} \\ & + \frac{(\bar{u}_1 - \bar{u}_2)}{h} \frac{\partial h}{\partial x} (-0.78 \bar{u}_1 + 0.38 \bar{u}_2) \\ & + \frac{1}{\text{Re}} \left( -1.98 \frac{\partial^2 \bar{u}_1}{\partial x^2} + 5.23 \frac{\partial^2 \bar{u}_2}{\partial x^2} \right). \end{aligned} \quad (17c)$$

Equation (17a) is a direct consequence of conservation of fluid. The momentum equations (17b)–(17c) include the effects of gravity  $\tan \theta - \partial h / \partial x$ , viscous drag  $\bar{u}_j / h^2$ , advection  $\bar{u}_j \partial \bar{u}_i / \partial x$ , dispersion  $\partial^2 \bar{u}_j / \partial x^2$ , and other viscous terms, such as  $\partial h / \partial x \partial \bar{u}_j / \partial x$ . Compared with the one-layer models (Prokopiou et al. 1991a, Roberts 1997, Ruyer-Quil & Manneville 1998, e.g.), the two-layer model (17b)–(17c) ensures more subtle effects and resolves more internal modes. These internal modes are necessary for a more generic microscale simulation in the gap-tooth scheme over that initiated for wave-like systems by Cao & Roberts (2014).

## 2.4 Eigenanalysis of the microscale model

This section linearly analyses the two-layer model (17). Linear analysis indicates that an unphysical instability appears for high wavenumber. Cao (2014) explored

three methods to avoid such instability: only resolving low wavenumbers; adding high order dissipation terms; and introducing a regularising operator. We implemented, recommend and describe the last.

**Linear analysis of the two-layer model** Consider the modelled fluid film flow with two artificial layers on a flat plate with slope  $\tan \theta$ . The fluid shear flow has an equilibrium with thickness  $h = 1$ , without loss of generality. The model (17), assuming  $\partial_t = \partial_x = 0$ , simplifies to

$$\begin{aligned} 0.826 \tan \theta + \frac{1}{\text{Re}} (-19.3\bar{u}_1 + 6.98\bar{u}_2) &= 0, \\ 1.002 \tan \theta + \frac{1}{\text{Re}} (6.98\bar{u}_1 - 5.36\bar{u}_2) &= 0, \end{aligned}$$

which predicts an equilibrium of layer mean velocities

$$\bar{u}_1 = 0.209 \text{Re} \tan \theta \quad \text{and} \quad \bar{u}_2 = 0.459 \text{Re} \tan \theta. \quad (18)$$

Impose small perturbations to this equilibrium and seek solutions in the form

$$\begin{aligned} h &= 1 + \hat{h} \exp(\lambda t + ikx), \\ \bar{u}_1 &= 0.209 \text{Re} \tan \theta + \hat{u}_1 \exp(\lambda t + ikx), \\ \bar{u}_2 &= 0.459 \text{Re} \tan \theta + \hat{u}_2 \exp(\lambda t + ikx), \end{aligned} \quad (19)$$

for growth rate  $\lambda$  (possibly complex) and nondimensional wavenumber  $k$ .

Substitute the form (19) into the model (17), equate coefficients and derive the linear problem

$$\lambda \begin{bmatrix} \hat{h} \\ \hat{u}_1 \\ \hat{u}_2 \end{bmatrix} = M \begin{bmatrix} \hat{h} \\ \hat{u}_1 \\ \hat{u}_2 \end{bmatrix},$$

where the coefficient matrix  $M$  is

$$\begin{bmatrix} -0.334 \tan \theta \text{Re} ik & -0.5ik & -0.5ik \\ -(0.826 + 0.0259 \tan \theta \text{Re})ik & \frac{1}{\text{Re}}(-19.3 + 3.84k^2) - 0.244 \tan \theta \text{Re} ik & \frac{1}{\text{Re}}(6.98 - 2.52k^2) - 0.088 \tan \theta \text{Re} ik \\ -(1.002 + 0.0029 \tan \theta \text{Re})ik & \frac{1}{\text{Re}}(6.98 + 1.98k^2) + 0.935 \tan \theta \text{Re} ik & \frac{1}{\text{Re}}(-5.36 - 5.23k^2) - 0.526 \tan \theta \text{Re} ik \end{bmatrix}. \quad (20)$$

The coefficient matrix  $M$  has characteristic equation

$$\lambda^3 + \lambda^2 \left[ 1.114 \tan \theta \text{Re} ik + \frac{1}{\text{Re}} (1.39k^2 + 24.66) \right]$$

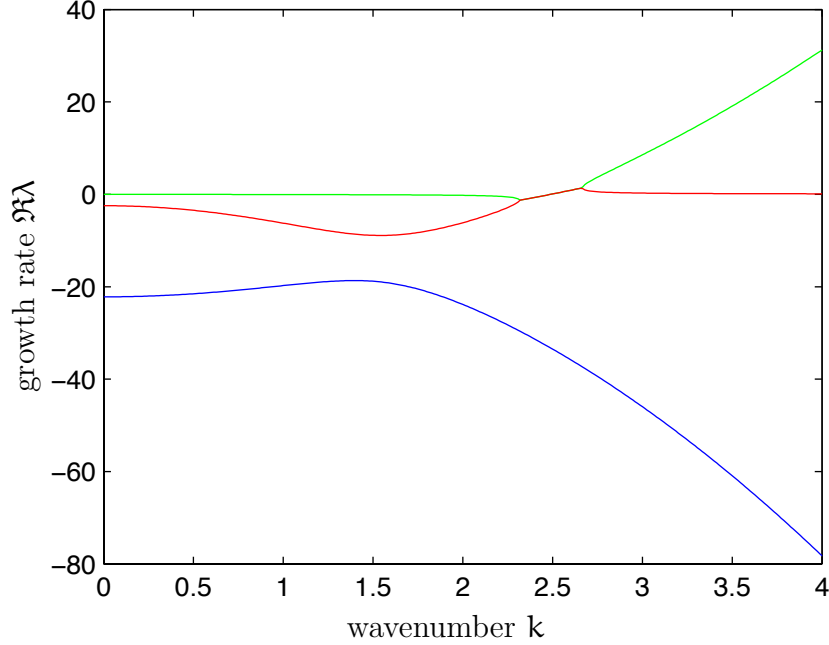


Figure 2: The growth rate  $\mathfrak{R}\lambda$  varies with the nondimensional wavenumber  $k$  from the characteristic equation (21) of the model (17). The slope of the plate is  $\tan \theta = 0$ . The Reynolds number is  $\text{Re} = 1$ . An unphysical instability appears for high nondimensional wavenumber  $k > 2.5$ . The little interval near  $k = 2.5$  is due to the numerical error.

$$\begin{aligned}
& -\lambda \left[ 0.476 \tan^2 \theta \text{Re}^2 k^2 + \tan \theta k (-2.265 i k^2 - 14.03 i - 0.0144 \text{Re} k) \right. \\
& \left. + 15.09 \frac{1}{\text{Re}^2} k^4 - 0.914 k^2 - 84.13 \frac{1}{\text{Re}^2} k^2 - 54.73 \frac{1}{\text{Re}^2} \right] \\
& - \left[ 0.0725 \tan^3 \theta \text{Re}^3 i k^3 + \tan^2 \theta \text{Re} k^2 (-0.0191 \text{Re} i k + 0.615 k^2 + 1.908) \right. \\
& \left. + \tan \theta \frac{1}{\text{Re}} k (5.19 i k^4 - 0.682 \text{Re}^2 i k^2 - 28.94 i k^2 - 18.83 i - 0.841 \text{Re} k^3 \right. \\
& \left. - 0.198 \text{Re} k) + \frac{1}{\text{Re}} k^2 (0.209 k^2 - 18.26) \right] = 0. \tag{21}
\end{aligned}$$

Figure 2 plots the growth rates  $\mathfrak{R}\lambda$  versus the nondimensional wavenumber  $k$  from equation (21). All the values represented by the blue curve are negative which nicely reflects viscous decay of lateral shear modes. When the nondimensional wavenumber  $k < 2.5$ , the values represented by the red curve are negative (viscous decay), and by the green curve are zeros (conservation of fluid). But when the nondimensional wavenumber  $k > 2.5$ , the green curve increases to positive which implies that instability arises in the system. This instability is nothing to do with physical instabilities, for example, found by [Chen \(1993\)](#), who found the instability of the two liquid films down an inclined plate due to the different viscosity at the

interface of the two layer flow and on the free surface. Here the instability arises at high wavenumber, a wavelength comparable to the thickness of the fluid, whereas our modelling is accurate for low wavenumber, long length scales.

**Consistently avoid the instability** We introduce a regularising operator to stabilise the unphysical instability. For the momentum equations (17b)–(17c), consider applying the regularising operator  $\mathcal{L} = 1 - C\partial_x(h^2\partial_x)$  to both sides of both PDEs. The coefficient  $C$  is positive. The reason for using  $h^2$  in the regularising operator  $\mathcal{L}$  is to be dimensionally consistent which means we can cancel the  $h^{-2}$  in the drag terms in equations (17b)–(17c) and also ensure the regularising operator  $\mathcal{L}$  is self-adjoint. This regularising operator generates dissipation effects to counteract the positive growth rates. The computer algebra of Appendix A applies the regularising operator to the momentum PDEs (17b)–(17c), and gives the PDEs, in term of the regularising parameter  $C$ ,

$$\frac{\partial h}{\partial t} = -0.5 \left( \frac{\partial h \bar{u}_1}{\partial x} + \frac{\partial h \bar{u}_2}{\partial x} \right), \quad (22a)$$

$$\begin{aligned} \mathcal{L} \frac{\partial \bar{u}_1}{\partial t} &\approx 0.826 \left( \tan \theta - \frac{\partial h}{\partial x} \right) \\ &+ \frac{1}{\text{Re}} \left( -19.3 \frac{\bar{u}_1}{h^2} + 6.98 \frac{\bar{u}_2}{h^2} \right) \\ &- 1.48 \bar{u}_1 \frac{\partial \bar{u}_1}{\partial x} - 0.225 \bar{u}_2 \frac{\partial \bar{u}_2}{\partial x} + 0.142 \bar{u}_2 \frac{\partial \bar{u}_1}{\partial x} + 0.0728 \bar{u}_1 \frac{\partial \bar{u}_2}{\partial x} \\ &+ \frac{(\bar{u}_1 - \bar{u}_2)}{h} (-0.25 \bar{u}_1 + 0.34 \bar{u}_2) \frac{\partial h}{\partial x} \\ &+ \frac{1}{\text{Re}} (-3.84 + 19.3C) \frac{\partial^2 \bar{u}_1}{\partial x^2} + \frac{1}{\text{Re}} (2.52 - 6.98C) \frac{\partial^2 \bar{u}_2}{\partial x^2}, \end{aligned} \quad (22b)$$

$$\begin{aligned} \mathcal{L} \frac{\partial \bar{u}_2}{\partial t} &\approx 1.002 \left( \tan \theta - \frac{\partial h}{\partial x} \right) \\ &+ \frac{1}{\text{Re}} \left( 6.98 \frac{\bar{u}_1}{h^2} - 5.36 \frac{\bar{u}_2}{h^2} \right) \\ &- 1.25 \bar{u}_1 \frac{\partial \bar{u}_1}{\partial x} - 1.57 \bar{u}_2 \frac{\partial \bar{u}_2}{\partial x} + 0.768 \bar{u}_2 \frac{\partial \bar{u}_1}{\partial x} + 0.930 \bar{u}_1 \frac{\partial \bar{u}_2}{\partial x} \\ &+ \frac{(\bar{u}_1 - \bar{u}_2)}{h} \frac{\partial h}{\partial x} (-0.78 \bar{u}_1 + 0.38 \bar{u}_2) \\ &+ \frac{1}{\text{Re}} (-1.98 - 6.98C) \frac{\partial^2 \bar{u}_1}{\partial x^2} + \frac{1}{\text{Re}} (5.23 + 5.36C) \frac{\partial^2 \bar{u}_2}{\partial x^2}. \end{aligned} \quad (22c)$$

Now we linearise this system (22) and derive the characteristic equation, parametrised by the regularising  $C$ ,

$$\lambda^3 + \lambda^2 \left[ 1.114 \tan \theta \text{Re} \, ik + \frac{1}{\text{Re}} (1.39k^2 + 24.66) + 24.66 \frac{1}{\text{Re}} Ck^2 \right]$$

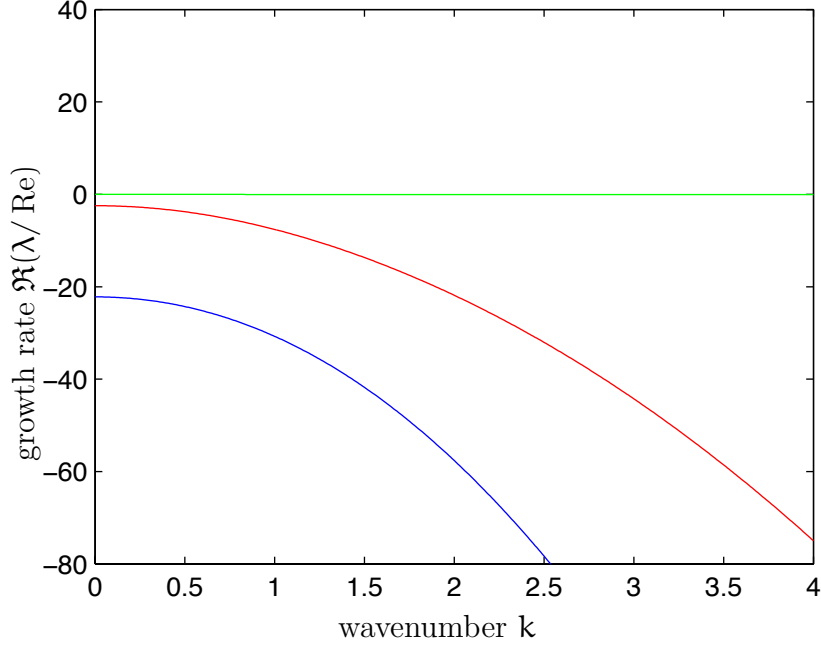


Figure 3: Plot of the growth rate  $\Re\lambda$  varying with the nondimensional wavenumber  $k$ . The coefficient  $C = 0.5$  in the regularising operator  $\mathcal{L}$ . The slope of the plate is  $\tan \theta = 0$ . The Reynolds number is  $\text{Re} = 1$ .

$$\begin{aligned}
& -\lambda \left[ 0.476 \tan^2 \theta \text{Re}^2 k^2 + \tan \theta k (-2.265 i k^2 - 14.03 i - 0.0144 \text{Re} k) \right. \\
& + 15.09 \frac{1}{\text{Re}^2} k^4 - 0.914 k^2 - 84.13 \frac{1}{\text{Re}^2} k^2 - 54.73 \frac{1}{\text{Re}^2} \\
& \left. - 14.03 C \tan \theta i k^3 - \frac{1}{\text{Re}^2} (54.73 C^2 k^4 + 84.13 C k^4 + 109.46 C k^2) \right] \\
& - \left[ 0.0725 \tan^3 \theta \text{Re}^3 i k^3 + \tan^2 \theta \text{Re} k^2 (-0.0191 \text{Re} i k + 0.615 k^2 + 1.908) \right. \\
& + \tan \theta \frac{1}{\text{Re}} k (5.19 i k^4 - 0.682 \text{Re}^2 i k^2 - 28.94 i k^2 - 18.83 i - 0.841 \text{Re} k^3 \\
& - 0.198 \text{Re} k) + \frac{1}{\text{Re}} k^2 (0.209 k^2 - 18.26) + \frac{1}{\text{Re}} (-18.83 C^2 \tan \theta i k^4 \\
& - 28.94 C \tan \theta i k^4 - 37.65 C \tan \theta i k^2 - 18.26 C k^3) + 1.908 C \tan^2 \theta \text{Re} k^3 \\
& \left. - 0.198 C \tan \theta k^3 \right] = 0. \tag{23}
\end{aligned}$$

Figure 3 plots the growth rate  $\Re\lambda$  varying with the nondimensional wavenumber  $k$  from the characteristic equation (23) for parameter  $C = 0.5$  in the regularising operator  $\mathcal{L}$ . That there is no positive growth rate demonstrates that no instability occurs, even for the high wavenumber. The decay rates represented by the blue and red curves grow quickly for large wavenumber. Numerical checks indicate that the regularising coefficient  $C > 0.17$  to eliminate the unphysical instabilities. This method is flexible through the wide range of choice of the positive coefficient  $C$

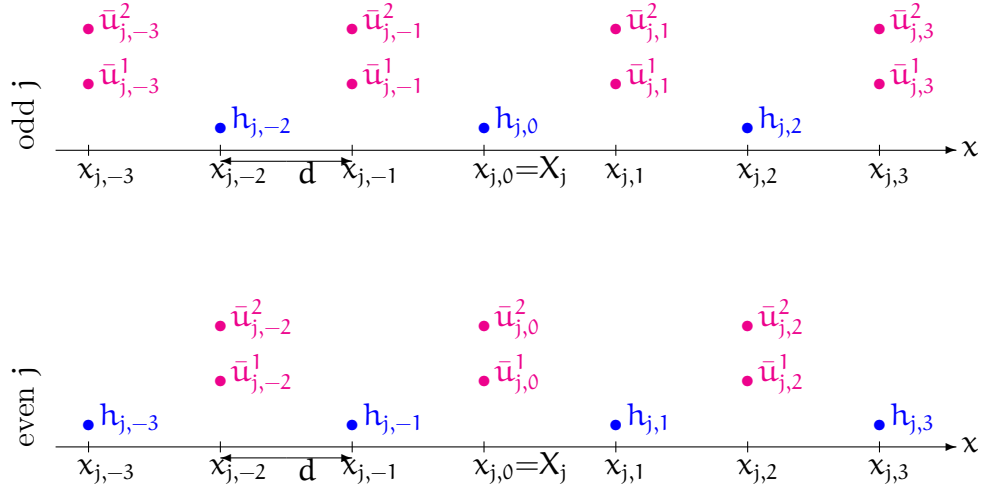


Figure 4: Scheme of the staggered grid points of the depth  $h_{j,i}$  (blue points) and the mean velocities  $\bar{u}_{j,i}^1$  and  $\bar{u}_{j,i}^2$  (magenta points) at the  $i$ th micro-grid point on the odd  $j$ th patch (top) and the even  $j$ th patch (bottom). This diagram show the cases for  $n = 5$  interior grid points in each patch ( $n' = 3$ ).

in the regularising operator  $\mathcal{L}$ . No high order derivatives, such as  $h^2 \partial^4 \bar{u}_1 / \partial x^4$ , appear with this regularising method. Thus, introducing the regularising operator  $\mathcal{L}$  usefully stabilises the model, and hereafter we implement the numerical simulations of the model (22) with the regularising coefficient  $C = 0.5$ .

### 3 Gap-tooth simulation of the two layer thin fluid flow

This section focuses on implementing the gap-tooth simulation of the thin fluid flow. This section uses the two-layer model (22) as the microscale simulator within patches. Coupling conditions (27a)–(27d) and (30) are developed to couple patches together.

Let us focus on one patch, the  $j$ th patch. Figure 4 shows the staggered grid for the depth  $h_{j,i}$  (blue points) and the layer mean velocities  $\bar{u}_{j,i}^1$  and  $\bar{u}_{j,i}^2$  (magenta points) at the  $i$ th micro-grid point ( $i = -n', \dots, n'$  for  $n' := (n + 1)/2$ ) on the  $j$ th patch. The superscripts correspond to the two mean velocities  $\bar{u}_1$  and  $\bar{u}_2$  on a patch. Let each of  $m$  patches be centred on equi-spaced macroscale grid points  $x = X_j = jD$ , where  $D = L/m$  is the macroscale spacing and  $L$  is the length of the whole domain. Each patch has relatively small width  $l$ . Assume each patch has a total of  $n$  microscale interior grid points, excluding the two edge grid points, so the microscale spatial step  $d = l/(n + 1)$ . Let each patch around a macroscale grid point  $X_j$  execute a microscale simulator.



The microscale simulator (22) is a straightforward second order differential equations. Approximate the PDEs (22) on the  $j$ th patch with centred differences in microscale space of  $\mathbf{d}$ . shown in Figure 4. Use Matlab `ode15s` for continuous time integration. The dominant error comes from the macroscale coupling between patches, not the microscale discretisation (Cao 2014, e.g.).

Define the mid patch point  $\mathbf{x}_{j,0} = \mathbf{X}_j$ . Let the macroscale value  $\mathbf{H}_j = \mathbf{h}_j(\mathbf{X}_j, \mathbf{t})$  for the odd  $j$  and  $\mathbf{U}_j = (\bar{\mathbf{u}}_j^1(\mathbf{X}_j, \mathbf{t}) + \bar{\mathbf{u}}_j^2(\mathbf{X}_j, \mathbf{t}))/2$  for even  $j$ . The inter-patch coupling uses only these macroscale values.

### 3.1 Coupling conditions on the odd patches

This subsection develops the coupling conditions on the odd patches. The velocity values  $\bar{\mathbf{u}}_{j,\pm n}^1$  and  $\bar{\mathbf{u}}_{j,\pm n}^2$  at the edges of the odd patches are approximated by interpolation of  $\mathbf{U}_{j\pm 1}, \mathbf{U}_{j\pm 3}, \dots$  from neighbouring patches, which is ‘lifted’ (Kevrekidis & Samaey 2009, e.g.) by requiring that the microscale dynamics lie on the slow manifold.

The dynamics in the interior of each patch is given by the microscale simulator (22). The regularising operator  $\mathcal{L} = 1 - C\partial_x(h^2\partial_x)$  of the two layer mean velocities  $\bar{\mathbf{u}}_1(\mathbf{x}, \mathbf{t})$  and  $\bar{\mathbf{u}}_2(\mathbf{x}, \mathbf{t})$  on the odd  $j$ th patch requires more details. For the example of  $n = 5$ , Figure 4, for odd  $j$  the two momentum equations (22b)–(22c) are of the form

$$\mathcal{L} \begin{bmatrix} \partial \bar{\mathbf{u}}_{j,-3}^\ell / \partial \mathbf{t} \\ \partial \bar{\mathbf{u}}_{j,-1}^\ell / \partial \mathbf{t} \\ \partial \bar{\mathbf{u}}_{j,1}^\ell / \partial \mathbf{t} \\ \partial \bar{\mathbf{u}}_{j,3}^\ell / \partial \mathbf{t} \end{bmatrix} = \text{RHS}, \quad (24)$$

where the RHS refers to a finite difference discretisation of the right-hand sides of the two-layer PDEs (22), and the superscript  $\ell = 1, 2$  for the lower and upper layer. The regularising operator  $\mathcal{L}$  has the matrix form, for the example  $n = 5$  case, of

$$\mathcal{L} = \frac{1}{4\mathbf{d}^2} \begin{bmatrix} -C\mathbf{h}_{j,-2}^2 & 1 + C(\mathbf{h}_{j,-2}^2 + \mathbf{h}_{j,0}^2) & -C\mathbf{h}_{j,0}^2 & 0 \\ 0 & -C\mathbf{h}_{j,0}^2 & 1 + C(\mathbf{h}_{j,0}^2 + \mathbf{h}_{j,2}^2) & -C\mathbf{h}_{j,2}^2 \end{bmatrix}, \quad (25)$$

where  $\mathbf{d}$  is the microscale spacial step. The values of  $\bar{\mathbf{u}}_{j,\pm n}^\ell$  are at the edges of the  $j$ th patch. Recall that the macroscale mean velocity  $\mathbf{U}_j(\mathbf{t}) = (\bar{\mathbf{u}}_j^1(\mathbf{X}_j, \mathbf{t}) + \bar{\mathbf{u}}_j^2(\mathbf{X}_j, \mathbf{t}))/2$  for the even  $j$  are known. Thus, this section completes the set of equations by finding the unknown microscale values  $\partial \bar{\mathbf{u}}_{j,\pm n}^\ell / \partial \mathbf{t}$  and  $\bar{\mathbf{u}}_{j,\pm n}^\ell$  from the known macroscale values  $\mathbf{U}_j$ .

The challenge is to deduce microscale values appropriate to the macroscale structures. E & Engquist (2003), E et al. (2007) and Malecha et al. (2013) studied a heterogeneous multiscale method (HMM). The HMM contains two main components: an overall macroscale scheme for the macroscale variables and estimating the missing macroscale data by the microscale model. A compression operator  $\mathbf{Q}$

and a reconstruction operator  $R$  are defined to satisfy  $Q\bar{u}_j = \mathbf{U}_j$ ,  $R\mathbf{U}_j = \bar{u}_j$  and  $QR\mathbf{U}_j = \mathbf{U}_j$ , where  $\bar{u}_j$  is the microscale variable and  $\mathbf{U}_j$  the macroscale variable. Such compression and reconstruction operators combine the microscale and macroscale variables. [Kevrekidis et al. \(2003\)](#), [Samaey, Roose & Kevrekidis \(2005\)](#) and [Samaey et al. \(2009\)](#) defined a coarse time-stepper by introducing a *lifting operator* and a corresponding *restriction operator* which transform between the microscale and macroscale variables. These works provide the methods to relate the microscale and macroscale.

This section analogously constructs a lifting operator to give the patch edge values of  $\bar{u}_{j,\pm n}^\ell$  and  $\partial\bar{u}_{j,\pm n}^\ell/\partial t$  in terms of the macroscale mean velocity  $\mathbf{U}_j$  by assuming the system lies on the one-layer slow manifold. Recall that the one-layer mean velocity  $\bar{u}(X_j, t) = \mathbf{U}_j = (\bar{u}_{j,0}^1 + \bar{u}_{j,0}^2)/2$ . One constraint on the lifting is the coupling conditions ([Cao & Roberts 2013](#), eq. (11)) that give a linear, cubic or quintic approximation for the one layer mean velocity, such as the quintic

$$\begin{aligned}\bar{u}(X_j \pm rD, t) &= \frac{1}{2} (\mathbf{U}_{j+1} + \mathbf{U}_{j-1}) \pm \frac{r}{2} (\mathbf{U}_{j+1} - \mathbf{U}_{j-1}) \\ &+ \frac{1}{16} (-1 + r^2) (\mathbf{U}_{j+2} - \mathbf{U}_{j+1} - \mathbf{U}_{j-1} + \mathbf{U}_{j-2}) \\ &\pm \frac{1}{48} (-r + r^3) (\mathbf{U}_{j+2} - 3\mathbf{U}_{j+1} + 3\mathbf{U}_{j-1} - \mathbf{U}_{j-2}).\end{aligned}\quad (26)$$

The other requirement is that the patch be on the slow manifold of macroscale waves. The following section 3.3 details the slow manifold of the two-layer model (22b)–(22c) in term of the mean velocity  $\bar{u}$ . For example and for simplicity, truncate the slow manifold description (32) and (34a)–(34b) to errors  $\mathcal{O}(\epsilon^2)$  and obtain the values of  $\bar{u}_{j,\pm n}^\ell$  and  $\partial\bar{u}_{j,\pm n}^\ell/\partial t$  on the odd  $j$ th patch as

$$\bar{u}_{j,\pm n}^1 = 0.587\bar{u}(X_j \pm rD, t) + 0.0129 \operatorname{Re} \tan \theta, \quad (27a)$$

$$\bar{u}_{j,\pm n}^2 = 1.413\bar{u}(X_j \pm rD, t) - 0.0129 \operatorname{Re} \tan \theta, \quad (27b)$$

$$\frac{\partial\bar{u}_{j,\pm n}^1}{\partial t} = -1.482 \frac{1}{\operatorname{Re}} \frac{1}{h^2} \bar{u}(X_j \pm rD, t) + 0.489 \tan \theta, \quad (27c)$$

$$\frac{\partial\bar{u}_{j,\pm n}^2}{\partial t} = -3.526 \frac{1}{\operatorname{Re}} \frac{1}{h^2} \bar{u}(X_j \pm rD, t) + 1.168 \tan \theta, \quad (27d)$$

where as a leading approximation we neglect the derivatives  $\partial/\partial x \approx 0$  in the slow manifold (34). Thus, equations (27a)–(27b) are the coupling conditions on the odd patches.

## 3.2 Coupling conditions on the even patches

This subsection develops the coupling conditions on the patches with even  $j$ . The values  $h_{j,\pm n}$  at the edges of the even patches are approximated from the neighbouring macroscale grid values to give coupling conditions.

Simulate on each patch by the discretisation of the microscale PDEs (22). The regularising operator  $\mathcal{L} = 1 - C\partial_x(h^2\partial_x)$  of the two layer mean velocities  $\bar{u}_1(x, t)$  and  $\bar{u}_2(x, t)$  on the even  $j$ th patch requires more details. For example, we record here details for  $n = 5$  as in Figure 4; other  $n$  is a direct generalisation. We need to approximate the second spatial derivatives  $\partial_x^2$  in the left-hand and right-hand sides of the (22b)–(22c) at the positions  $x_{j,\pm 2}$ , which requires two virtual grid values  $\bar{u}_{j,\pm 4}^\ell$ . We set the values  $\bar{u}_{j,\pm 4}^\ell = \bar{u}_{j,\pm 2}^\ell$  on the slow manifold. Thus, in Figure 4, for even  $j$  the momentum equations (22b)–(22c) are of the form

$$\mathcal{L} \begin{bmatrix} \partial \bar{u}_{j,-4}^\ell / \partial t \\ \partial \bar{u}_{j,-2}^\ell / \partial t \\ \partial \bar{u}_{j,0}^\ell / \partial t \\ \partial \bar{u}_{j,2}^\ell / \partial t \\ \partial \bar{u}_{j,4}^\ell / \partial t \end{bmatrix} = \text{RHS}, \quad (28)$$

where the regularising operator  $\mathcal{L}$  is discretised in the matrix form

$$\frac{1}{4d^2} \begin{bmatrix} -Ch_{j,-3}^2 & 1 + C(h_{j,-3}^2 + h_{j,-1}^2) & -Ch_{j,-1}^2 & 0 & 0 \\ 0 & -Ch_{j,-1}^2 & 1 + C(h_{j,-1}^2 + h_{j,1}^2) & -Ch_{j,1}^2 & 0 \\ 0 & 0 & -Ch_{j,1}^2 & 1 + C(h_{j,3}^2 + h_{j,1}^2) & -Ch_{j,3}^2 \end{bmatrix}, \quad (29)$$

and where the RHS refers to a discretisation of the right-hand sides of the momentum equations (22b)–(22c), the superscript  $\ell = 1, 2$  for the lower and upper layer, and  $d$  is the microscale spatial step.

The regularising operator  $\mathcal{L}$  and the RHSs need the values of  $h_{j,\pm n}$ . Coupling conditions approximate the values of  $h_{j,\pm n}$  by interpolating the neighbouring macroscale values of  $H_{j\pm 1}, H_{j\pm 2}, \dots$ . The coupling conditions (Cao & Roberts 2013, eq. (11)) give a linear, cubic or quintic interpolation, such as the quintic

$$\begin{aligned} h_{j,\pm n} &= h(X_j \pm rD, t) = \frac{1}{2} (H_{j+1} + H_{j-1}) \pm \frac{r}{2} (H_{j+1} - H_{j-1}) \\ &+ \frac{1}{16} (-1 + r^2) (H_{j+2} - H_{j+1} - H_{j-1} + H_{j-2}) \\ &\pm \frac{1}{48} (-r + r^3) (H_{j+2} - 3H_{j+1} + 3H_{j-1} - H_{j-2}), \end{aligned} \quad (30)$$

where  $r$  is the ratio of between the macroscale step and half of the width of a patch. Thus the interpolation (30), together with equations (27a)–(27b), couple the patches together over the macroscale domain.

### 3.3 The low order model of one layer flow

This section derives a slow manifold of the two-layer model (22b)–(22c) in terms of the mean velocity  $\bar{\mathbf{u}}$ . This slow manifold is used by sections 3.1–3.2 in order to lift the macroscale information to the microscale simulation on patches.

A fluid film model expressed in terms of the dynamics of *both* the fluid layer thickness and an overall lateral velocity (or momentum flux) is needed to resolve wave-like dynamics in many situations (Roberts & Li 2006): falling films (Nguyen & Balakotaiah 2000, Chang 1994b, p.110); wave transitions (Chang et al. 2002) to solitary waves (Ruyer-Quil & Manneville 2000); higher Reynolds number flows (Prokopiou et al. 1991b, Eqn.(19)); in rising film flow and a slot coater (Kheshgi 1989, Eqn.(37)); rivulets under a sloping cylinder (Alekseenko et al. 1996). A slow manifold model of our two layer model corresponds to these earlier models of the fluid dynamics.

Indeed our construction here generates a slow manifold, one-layer model of the fluid dynamics which is the same as that of Roberts (1997) (to the order of error of the analysis). The distinction is that here it is derived from the two-layer model, rather than the original fluid equations: this transitivity of modelling additionally validates the modelling process. For simplicity, we base the analysis upon a symmetric linear operator with slow eigenspace where the two layer velocities are in the ratio  $1 : 2$ . To derive the slow manifold of the two-layer model, we embed the physical model (22b)–(22c) into a family of artificial problems by using another artificial parameter  $\gamma'$ ,

$$-\frac{\partial \bar{\mathbf{u}}_1}{\partial t} + \text{RHS}_{(17b)} + (1 - \gamma') \frac{\text{Eu}}{\text{Re}} \frac{1}{h^2} (-4\bar{\mathbf{u}}_1 + 2\bar{\mathbf{u}}_2) = 0, \quad (31a)$$

$$-\frac{\partial \bar{\mathbf{u}}_2}{\partial t} + \text{RHS}_{(17c)} + (1 - \gamma') \frac{\text{Eu}}{\text{Re}} \frac{1}{h^2} (2\bar{\mathbf{u}}_1 - \bar{\mathbf{u}}_2) = 0, \quad (31b)$$

where  $\text{RHS}_{(17b)}$  and  $\text{RHS}_{(17c)}$  are the right-hand sides of the PDEs (17b)–(17c). The variable  $\text{Eu}$  denotes an artificial Euler parameter used to enhance convergence (van Dyke 1964, 1984, e.g.): computational experiments indicate that  $\text{Eu} = 9/2$  delivers good convergence in the artificial parameter  $\gamma'$ . When the parameter  $\gamma' = 1$ , the PDEs (31) recover the original PDEs (17b)–(17c). When the artificial parameter  $\gamma' = 0$ , the linear operator in the PDEs (31) is

$$\frac{\text{Eu}}{h^2 \text{Re}} \begin{bmatrix} -4 & 2 \\ 2 & -1 \end{bmatrix},$$

and it is this linear operator that guides effective recursive improvements of approximations to the original PDEs.

For a specific model we choose to truncate to errors  $\mathcal{O}(\bar{\mathbf{u}}^4 + \partial_x^4 + \theta^4, \gamma'^7)$ . Then executing the computer algebra in Appendix A and evaluating at the artificial parameter  $\gamma' = 1$ , leads to the slow manifold where the two layer velocities are

$$\bar{\mathbf{u}}_1 \approx 0.587\bar{\mathbf{u}} + 0.0129 \text{Re} h^2 \left( \tan \theta - \frac{\partial h}{\partial x} \right)$$

$$\begin{aligned}
& -0.0468h^2 \frac{\partial^2 \bar{u}}{\partial x^2} - 0.205h \frac{\partial h}{\partial x} \frac{\partial \bar{u}}{\partial x} + 0.0700h\bar{u} \frac{\partial^2 h}{\partial x^2} \\
& + \operatorname{Re} \left( 0.00465h^2 \bar{u} \frac{\partial \bar{u}}{\partial x} - 0.0115h\bar{u}^2 \frac{\partial h}{\partial x} - 0.0105h^3 \frac{\partial h}{\partial x} \frac{\partial^2 h}{\partial x^2} \right), \quad (32a)
\end{aligned}$$

$$\begin{aligned}
\bar{u}_2 \approx & 1.413\bar{u} - 0.0129 \operatorname{Re} h^2 \left( \tan \theta - \frac{\partial h}{\partial x} \right) \\
& + 0.0468h^2 \frac{\partial^2 \bar{u}}{\partial x^2} + 0.205h \frac{\partial h}{\partial x} \frac{\partial \bar{u}}{\partial x} - 0.0700h\bar{u} \frac{\partial^2 h}{\partial x^2} \\
& - \operatorname{Re} \left( 0.00465h^2 \bar{u} \frac{\partial \bar{u}}{\partial x} - 0.0115h\bar{u}^2 \frac{\partial h}{\partial x} - 0.0105h^3 \frac{\partial h}{\partial x} \frac{\partial^2 h}{\partial x^2} \right). \quad (32b)
\end{aligned}$$

Equations (32) are expressed in terms of the single layer depth-averaged velocity  $\bar{u}(x, t)$  and the water depth  $h(x, t)$ .

On the slow manifold (32), conservation of mass requires

$$\frac{\partial h}{\partial t} = -\frac{\partial h\bar{u}}{\partial x}. \quad (33)$$

The computer algebra in Appendix A differentiates equations (32) with respect to the time  $t$ , and gives the rate of change of the two layer velocities in term of the mean velocity  $\bar{u}$  and fluid depth  $h$  as

$$\begin{aligned}
\frac{\partial \bar{u}_1}{\partial t} \approx & 0.489 \left( \tan \theta - \frac{\partial h}{\partial x} \right) - 1.482 \frac{1}{\operatorname{Re}} \frac{\bar{u}}{h^2} - 0.904\bar{u} \frac{\partial \bar{u}}{\partial x} \\
& + \frac{1}{\operatorname{Re}} \left( 2.552 \frac{\partial^2 \bar{u}}{\partial x^2} + 3.077 \frac{1}{h} \frac{\partial h}{\partial x} \frac{\partial \bar{u}}{\partial x} - 0.650 \frac{\bar{u}}{h} \frac{\partial^2 h}{\partial x^2} \right) \\
& + \operatorname{Re} \left[ 0.0167h^3 \frac{\partial^2 \bar{u}}{\partial x^2} + 0.0438h^2 \frac{\partial h}{\partial x} \frac{\partial^2 h}{\partial x^2} + 0.0359h\bar{u} \left( \frac{\partial h}{\partial x} \right)^2 \right] \\
& - \operatorname{Re} \tan \theta \left( 0.0298h\bar{u} \frac{\partial h}{\partial x} + 0.0184h^2 \frac{\partial \bar{u}}{\partial x} \right), \quad (34a)
\end{aligned}$$

$$\begin{aligned}
\frac{\partial \bar{u}_2}{\partial t} \approx & 1.168 \left( \tan \theta - \frac{\partial h}{\partial x} \right) - 3.526 \frac{1}{\operatorname{Re}} \frac{\bar{u}}{h^2} - 2.107\bar{u} \frac{\partial \bar{u}}{\partial x} \\
& + \frac{1}{\operatorname{Re}} \left( 5.701 \frac{\partial^2 \bar{u}}{\partial x^2} + 6.962 \frac{1}{h} \frac{\partial h}{\partial x} \frac{\partial \bar{u}}{\partial x} - 0.312 \frac{\bar{u}}{h} \frac{\partial^2 h}{\partial x^2} \right) \\
& - \operatorname{Re} \left[ 0.00819h^3 \frac{\partial^2 \bar{u}}{\partial x^2} + 0.0482h^2 \frac{\partial h}{\partial x} \frac{\partial^2 h}{\partial x^2} + 0.0875h\bar{u} \left( \frac{\partial h}{\partial x} \right)^2 \right] \\
& + \operatorname{Re} \tan \theta \left( 0.0847h\bar{u} \frac{\partial h}{\partial x} + 0.0355h^2 \frac{\partial \bar{u}}{\partial x} \right). \quad (34b)
\end{aligned}$$

Equations (34) provide needed microscale information from the macroscale fields  $\bar{u}$  and  $h$ .

The computer algebra in Appendix A simultaneously determines the evolution on the slow manifold of the one-layer model. The momentum equation is

$$\frac{\partial \bar{u}}{\partial t} \approx 0.829 \left( \tan \theta - \frac{\partial h}{\partial x} \right) - 2.504 \frac{1}{\text{Re}} \frac{\bar{u}}{h^2} - 1.505 \bar{u} \frac{\partial \bar{u}}{\partial x} - 0.151 \frac{\bar{u}^2}{h} \frac{\partial h}{\partial x}. \quad (35)$$

This PDE (35) has the same terms as the low order model of Roberts (1997) [eq. (11)]. The coefficients of these terms are the same to a relative error of less than 2.2%. This agreement partially verifies that the two-layer model is a reasonable model of the fluid film flow.

## 4 Numerical gap-tooth simulations of the two layer thin fluid flow

This section explores the numerical gap-tooth simulation with the two-layer microscale simulator (22) and the patch coupling conditions (30) and (26)–(27). Numerical eigenvalues and simulations show that the gap-tooth scheme reasonably simulates the macroscopic dynamics of the fluid film flow.

Consider the thin fluid flow on a horizontal plate: that is, the mean slope  $\tan \theta = 0$ . Distribute  $m$  patches in the macroscale domain of length  $L = m\pi$ , so the distance between the neighbouring patches is  $D = L/m = \pi$ . Divide each patch into  $n + 1$  equal microscale intervals by  $n + 2$  grid points, then the distance between neighbouring microscale points is  $d = 2rD/(n + 1)$ , where  $r$  is the ratio between the half-width of each patch and the macroscale inter-patch distance  $D$ . We approximate the spatial derivatives in the right-hand side of the two-layer PDEs (22) by centred differences on the staggered microscale grids.

Figure 5 plots the growth rate  $\Re \lambda$  versus the frequency  $\Im \lambda$  in the gap-tooth simulation of the thin fluid flow. There are  $m = 10$  patches and  $n = 9$  microscale grids on a patch. The plate has a length  $L = m\pi \approx 31.4$ , so the distance between the neighbouring patches is  $D = L/m = 3.14$ . The ratio  $r = 1/6$ , so the microscale step on a patch is  $d = 2rD/(n + 1) \approx 0.17$ . The Reynolds number  $\text{Re} = 15$  and the coefficient in the regularising operator  $\mathcal{L}$  is  $C = 0.5$ . The negative growth rates imply the waves decay in time.

There are 90 pairs of eigenvalues for the system:

- the eigenvalues with large decay rates ( $\Re \lambda < -1$ ) and zero imaginary parts predominantly represent the viscous decay of the lateral shear modes;
- the eigenvalues with large decay rates ( $\Re \lambda < -1$ ) but with large imaginary parts ( $|\Im \lambda| > 2$ ) correspond to microscale waves within each patch; and
- the eigenvalues with small growth rates ( $|\Re \lambda| < 0.2$ ) in the red rectangle, zoomed in by Figure 6, represent the interesting macroscale wave-like dynamics. This set of ten eigenvalues includes two groups of four eigenvalues

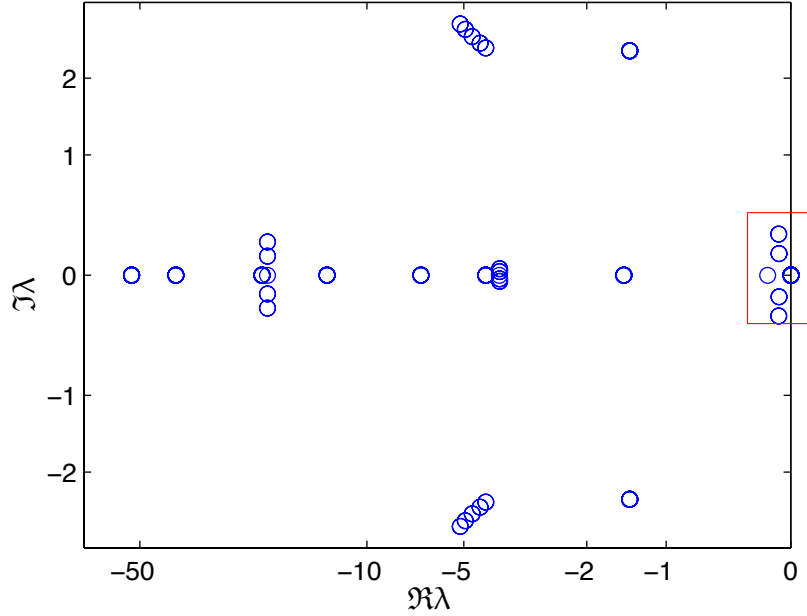


Figure 5: Plots of the growth rate  $\Re\lambda$  versus the frequency  $\Im\lambda$  in the gap-tooth simulation of the thin film flow (with nonlinear axis scaling) over horizontal plate. There are  $m = 10$  patches and  $n = 9$  microscale grid points within a patch. The Reynolds number  $Re = 15$  and the coefficient in the regularising operator  $\mathcal{L}$  is  $C = 0.5$ .

representing waves of wavenumbers 0.2 and 0.4, a zero eigenvalue representing conservation of water, and  $\lambda \approx -0.16$  representing the decay of homogeneous shear.

The pattern of eigenvalues seen in Figure 5 is typical over a wide range of parameters. It shows the emergence of the macroscale wave modes from among the fast microscale modes within each patch.

Simulations confirm the nonlinear dynamics of the gap-tooth scheme are appropriate. Figure 7 plots and compares the free surface of the thin film flow in a gap-tooth simulation and in the microscale simulation over the whole domain. Time integration invoked the Matlab `ode15s` function. There are  $m = 10$  patches and  $n = 9$  microscale grids on a patch. The  $t = 0$  graph shows that initially impose a perturbation  $0.2 \sin(2\pi/Lx)$  with small random noises to the equilibrium of fluid thickness one and initial layer mean velocities  $\bar{u}_1 = 0$  and  $\bar{u}_2 = 0.2$ , so the mean layer velocity  $\bar{u} = (\bar{u}_1 + \bar{u}_2)/2 = 0.1$ . The  $t = 2$  to  $t = 10$  graphs show that the microscale modes on a patch smooth quickly and the macroscale waves propagate and slowly decay, which agrees with the large decay rates of the microscale waves and small decay rates of the macroscale modes in Figure 5. Further numerical simulation shows that the macroscale waves decay to the equilibrium of thickness

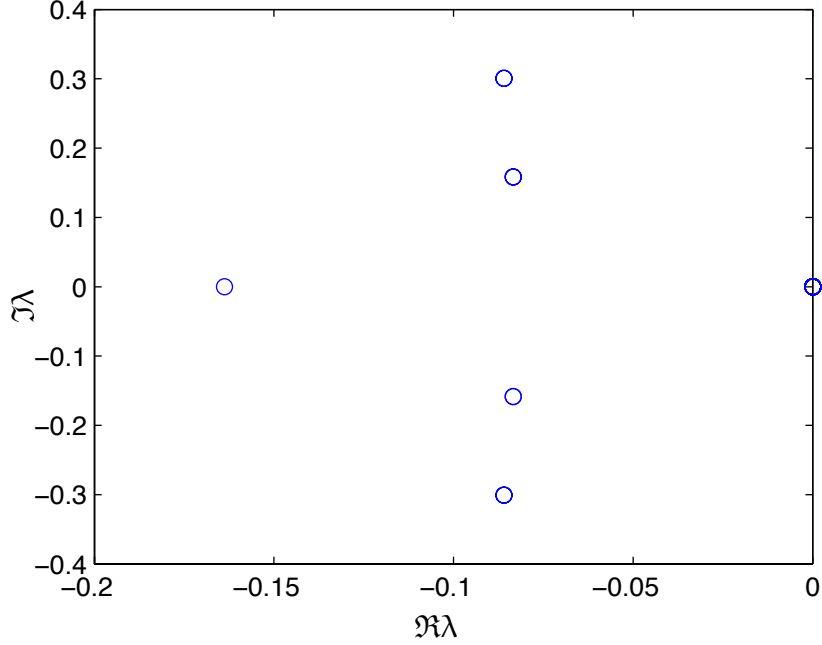


Figure 6: Zoom into the values in the red rectangle in Figure 5. These eigenvalues which represent the macroscale modes.

one after time  $t \approx 30$  for the Reynolds number  $Re = 15$ . When the Reynolds number  $Re$  becomes smaller, the macroscale waves decay faster to the equilibrium due to the stronger viscous effects. Figure 7 shows that the gap-tooth simulation agrees with the microscale simulation over the whole domain. The likely reason for the differences in  $t = 10$  graph is that the gap-tooth simulation near the water bore involves the error  $\mathcal{O}(D^2)$  for the macroscale step  $D = L/m \approx 3.14$ , while the microscale simulation on the whole macroscale domain involves the error  $\mathcal{O}(d^2)$  for the microscale step  $d = 2rD/(n+1) = 0.13$ : the ratio of these errors is  $\mathcal{O}(D^2/d^2) \approx 500$  showing the macroscale simulation is limited largely by the interpolation between patches. As the number of patches increases, the error  $\mathcal{O}(D^2)$  declines, and the gap-tooth simulation performs better. We show just  $m = 10$  patches here for clarity.

Figure 8 plots the corresponded layer mean velocities  $\bar{u}_1$  (blue) and  $\bar{u}_2$  (red) in the gap-tooth simulation and in the microscale simulation on the whole domain.

## 5 Conclusion

This work applies the gap-tooth scheme to the thin fluid flow with a derived novel two-layer model (22) being the microscale simulator. The two-layer model (22) provides more microscale modes, but without the full complexity of fully resolved vertical structures.



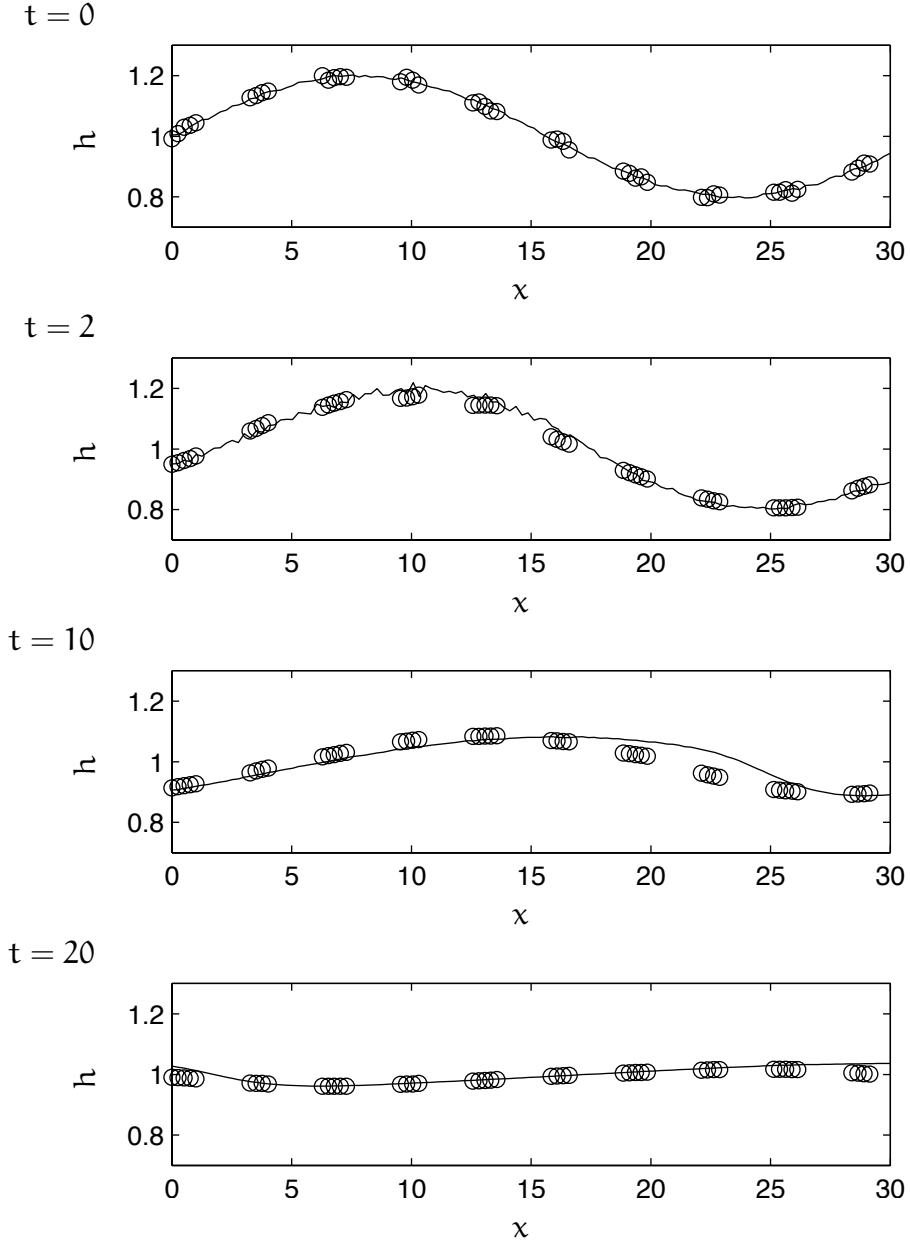


Figure 7: Plots of the fluid thickness of the thin fluid flow on the domain  $[0, 10\pi]$ : (circle) for the gap-tooth simulation; and (line) for microscale simulation on the whole domain. There are  $m = 10$  patches and  $n = 9$  microscale grids on a patch. The Reynolds number  $Re = 15$  and the regularising coefficient  $C = 0.5$ . The plate has a slope  $\tan \theta = 0$ . Figure 8 shows the corresponding fluid velocities.

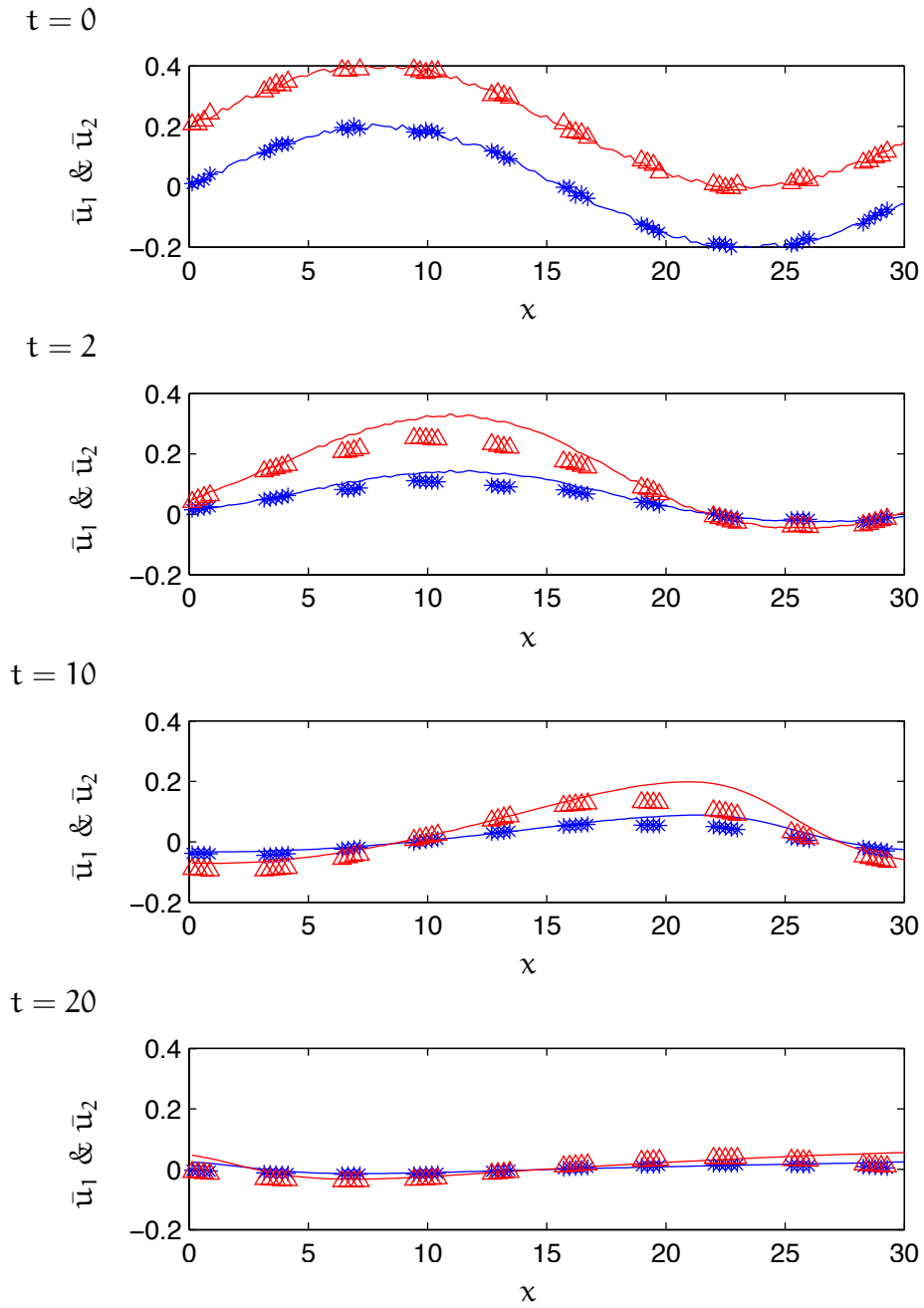


Figure 8: Plots of the layer mean velocities: (blue line) represents  $\bar{u}_1$  and (red line) represents  $\bar{u}_2$  in the microscale simulation over the whole domain; and (blue star) represents  $\bar{u}_1$  and (red triangle) represents  $\bar{u}_2$  in the gap-tooth simulation of the fluid film flow on the domain  $[0, 10\pi]$ . There are  $m = 10$  patches and  $n = 9$  microscale grids on a patch.

Based on centre manifold theory, section 2–2.4 derive the two-layer model (22) from the continuity and modified Navier–Stokes equations. The model (22) includes the effects of gravity, drag, advection and dispersion. The slow manifold of the two-layer model agrees with the one-layer model of thin film flow by Roberts (1997). Eigenvalues analysis in section 2.4 indicates unphysical instability appear, but a consistent regularising operator  $\mathcal{L}$  stabilises the model.

Then we simulate the thin fluid flow by new adaptations of the gap-tooth scheme with the two-layer model (22) being the microscale simulator. Section 3.3 algebraically derives the slow manifold of the two-layer model (22) in order to lift the macroscale information to the microscale simulation on patches. Then coupling conditions (30) and (27a)–(27b) are developed to couple the patches. Numerical eigenvalues in Figure 5–6 show that the macroscale modes decay slowly over the whole domain, while the microscale modes oscillate fast and decay quickly to quasi-equilibrium quickly. Non-zero frequencies  $\Im\lambda$  in Figure 6 indicate waves are supported on the free surface over the whole domain. Numerical simulations in Figure 7–8 show that the gap-tooth scheme with the two-layer model (22) being microscale simulator work well enough for the thin film flow. Future work is planned to build on this base in order to apply the gap-tooth scheme to the complicated microscale physics of turbulent, possibly ice covered, water waves, with the aim of empowering effective computation over very large lateral scales.

## References

- Alekseenko, S. V., Markovich, D. M. & Shtork, S. I. (1996), ‘Wave flow of rivulets on the outer surface of an inclined cylinder’, *Phys. Fluids* **8**, 3288–3299.
- Aulbach, B. & Wanner, T. (2000), ‘The Hartman–Grobman theorem for Caratheodory-type differential equations in Banach spaces’, *Nonlinear Analysis* **40**, 91–104. [http://dx.doi.org/10.1016/S0362-546X\(00\)85006-3](http://dx.doi.org/10.1016/S0362-546X(00)85006-3).
- Benjamin, T. B. (1957), ‘Wave formation in a laminar flow down an inclined plane’, *J. Fluid Mech.* **2**, 554–574. [doi:10.1017/S0022112057000373](https://doi.org/10.1017/S0022112057000373).
- Cao, M. (2014), Modelling environmental turbulent fluids and multiscale modelling couples patches of wave-like system, PhD thesis, School of Mathematical Sciences, University of Adelaide.
- Cao, M. & Roberts, A. J. (2013), Multiscale modelling couples patches of wave-like simulations, in S. McCue, T. Moroney, D. Mallet & J. Bunder, eds, ‘Proceedings of the 16th Biennial Computational Techniques and Applications Conference, CTAC-2012’, Vol. 54 of *ANZIAM J.*, pp. C153–C170. <http://journal.austms.org.au/ojs/index.php/ANZIAMJ/article/view/6137>.

- Cao, M. & Roberts, A. J. (2014), Multiscale modelling couples patches of nonlinear wave-like simulations, Technical report, [<http://http://arxiv.org/abs/1404.6317>].
- Chang, H.-C. (1987), ‘Evolution of nonlinear waves on vertically falling films—a normal form analysis’, *Chemical Engineering Science* **42**, 515–161. doi:10.1016/0009-2509(87)80014-3.
- Chang, H.-C. (1994a), ‘Wave evolution on a falling film’, *Annu. Rev. Fluid Mech.* **26**, 103–136. doi:10.1146/annurev.fl.26.010194.000535.
- Chang, H. C. (1994b), ‘Wave evolution on a falling film’, *Annu. Rev. Fluid Mech.* **26**, 103–136. <http://dx.doi.org/10.1146/annurev.fl.26.010194.000535>.
- Chang, H.-C., Demekhin, E. & Saprikin, S. S. (2002), ‘Noise-driven wave transitions on a vertically falling film’, *J. Fluid Mech.* **462**, 255–283. <http://dx.doi.org/10.1017/S0022112002008856>.
- Chen, K. (1993), ‘Wave formation in the gravitydriven lowreynolds number flow of two liquid films down an inclined plane’, *Physics of Fluids* **5**, 3038. doi:10.1063/1.858714.
- E, W. & Engquist, B. (2003), ‘The heterogeneous multiscale methods’, *Comm. Math. Sci.* **1**(1), 87–132. <http://projecteuclid.org/euclid.cms/1118150402>.
- E, W., Engquist, B., Li, X., Ren, W. & Vanden-Eijnden, E. (2007), ‘Heterogeneous Multiscale Methods: A Review’, *Communications in Computational Physics* **2**(3), 367–450. doi:10.1.1.225.9038.
- Gear, C. W., Li, J. & Kevrekidis, I. G. (2003), ‘The gap-tooth method in particle simulations’, *Phys. Lett. A* **316**, 190–195. <http://dx.doi.org/10.1016/j.physleta.2003.07.004>.
- Hou, T. Y., Yang, D. & Ran, H. (2008), ‘Multiscale analysis and computation for the three-dimensional incompressible Navier-Stokes equations’, *Multiscale Modelling and Simulation* **6**(4), 1317–1346. doi:10.1137/070682046.
- Kevrekidis, I. G., Gear, G. W., Hyman, J. M., Kevrekidis, P. G., Runborg, O. & Theodoropoulos, C. (2003), ‘Equation-free, coarse-grained multiscale computation: enabling microscopic simulators to perform system-level analysis’, *Comm. Math. Sci.* **1**(4), 715–762. <http://projecteuclid.org/euclid.cms/1119655353>.
- Kevrekidis, I. G. & Samaey, G. (2009), ‘Equation-free multiscale computation: Algorithms and applications’, *Annu. Rev. Phys. Chem.* **60**, 321–44. doi:10.1146/annurev.physchem.59.032607.093610.

- Kheshgi, H. S. (1989), ‘Profile equations for film flows at moderate Reynolds numbers’, *AIChE Journal* **35**, 1719–1727. <http://dx.doi.org/10.1002/aic.690351017>.
- Malecha, Z., Chini, G. & Julien, K. (2013), ‘A multiscale algorithm for simulating spatially-extended Langmuir circulation dynamics’, *J. Comput. Phys.* . [doi:10.1016/j.jcp.2013.07.003](https://doi.org/10.1016/j.jcp.2013.07.003).
- Nguyen, L. T. & Balakotaiah, V. (2000), ‘Modeling and experimental studies of wave evolution on free falling viscous films’, *Phys. Fluids* **12**, 2236–2256.
- Potzsche, C. & Rasmussen, M. (2006), ‘Taylor approximation of integral manifolds’, *Journal of Dynamics and Differential Equations* **18**(2), 427–460. [doi:10.1007/s10884-006-9011-8](https://doi.org/10.1007/s10884-006-9011-8).
- Prokopiou, T., Cheng, M. & Chang, H. C. (1991a), ‘Long waves on inclined films at high reynolds number’, *Journal of Fluid Mechanics* **222**, 665–691. [doi:10.1017/S002211209100126X](https://doi.org/10.1017/S002211209100126X).
- Prokopiou, T., Cheng, M. & Chang, H. C. (1991b), ‘Long waves on inclined films at high Reynolds number’, *J. Fluid Mech.* **222**, 665–691.
- Roberts, A. J. (1988), ‘The application of centre-manifold theory to the evolution of systems which vary slowly in space’, *J. Austral. Math. Soc. Ser. B* **29**, 480–500. [doi:10.1017/S0334270000005968](https://doi.org/10.1017/S0334270000005968).
- Roberts, A. J. (1997), ‘Low-dimensional models of thin film fluid dynamics’, *Phys. Letts. A* **212**, 63–72. [doi:10.1016/0375-9601\(96\)00040-0](https://doi.org/10.1016/0375-9601(96)00040-0).
- Roberts, A. J. (1998), An accurate model of thin 2d fluid flows with inertia on curved substrates, in ‘Free-surface flows with viscosity’, Vol. 16 of *Advances in Fluid Mechanics Series*, Comput Mech Pub, chapter 3, pp. 69–88.
- Roberts, A. J. (2013), Macroscale, slowly varying, models emerge from the microscale dynamics in long thin domains, Technical report, [<http://arxiv.org/abs/1310.1541>].
- Roberts, A. J. & Kevrekidis, I. G. (2005), ‘Higher order accuracy in the gap-tooth scheme for large-scale dynamics using microscopic simulators’, *ANZIAM Journal* **46**, C637–C657. <http://journal.austms.org.au/ojs/index.php/ANZIAMJ/article/view/981/847>.
- Roberts, A. J. & Li, Z. (2006), ‘An accurate and comprehensive model of thin fluid flows with inertia on curved substrates’, *J. Fluid Mech.* **553**, 33–73. <http://dx.doi.org/10.1017/S0022112006008640>.

- Roberts, A. J., Mei, Z. & Li, Z. (2002), ‘Modelling the dynamics of turbulent floods’, *SIAM J. on Applied Mathematics* **63**, 423–458. doi:10.1137/S0036139999358866.
- Roy, R. V., Roberts, A. J. & Simpson, M. E. (2002), ‘A lubrication model of coating flows over a curved substrate in space’, *J. Fluid Mech.* **454**, 235–261. doi:10.1017/S0022112001007133.
- Ruyer-Quil, C. & Manneville, P. (1998), ‘Modeling film flows down inclined planes’, *Eur. Phys. J. B* **6**, 277–292. doi:10.1007/s100510050550.
- Ruyer-Quil, C. & Manneville, P. (2000), ‘Improved modeling of flows down inclined planes’, *Eur. Phys. J. B* **15**, 357–369. <http://www.springerlink.com/link.asp?id=9ffp55pnhqkxe0lk>.
- Samaey, G., Kevrekidis, I. G. & Roose, D. (2005), ‘The gap-tooth scheme for homogenization problems’, *SIAM Multiscale Modeling and Simulation* **4**, 278–306. <http://dx.doi.org/10.1137/030602046>.
- Samaey, G., Roberts, A. J. & Kevrekidis, I. G. (2009), *Equation-free computation: an overview of patch dynamics*, Vol. 8 of Multiscale Methods, Oxford Scholarship Online Monographs. doi:10.1093/acprof:oso/9780199233854.003.0008.
- Samaey, G., Roose, D. & Kevrekidis, I. G. (2005), ‘The gap-tooth scheme for homogenization problems’, *Multiscale Modelling and Simulation* **4**, 278–306. doi:10.1137/030602046.
- van Dyke, M. (1964), ‘Higher approximations in boundary-layer theory. Part 3. parabola in uniform stream’, *J. Fluid Mech.* **19**, 145–159.
- van Dyke, M. (1984), ‘Computer-extended series’, *Annu. Rev. Fluid Mech.* **16**, 287–310.
- Weinstein, S. J. & Ruschak, K. J. (2004), ‘Coating flows’, *Annu. Rev. Fluid Mech.* **36**, 29–53. doi:10.1146/annurev.fluid.36.050802.122049.

## A Ancillary computer algebra program

This appendix lists the computer algebra to derive a two-layer model of the viscous layer of fluid. Denote fluid thickness  $h(\mathbf{x}, t)$  by  $h$ , layer mean velocities  $\bar{u}_j(\mathbf{x}, t)$  by  $uu_j$  for the lower layer  $j = 1$  and upper layer  $j = 2$ , and their evolution  $\partial h / \partial t = gh$  and  $\partial \bar{u}_j / \partial t = gu_j$ . The Reynolds number is  $re$ , and the coefficients of lateral and normal gravitational forcing are  $grx$  and  $grz:=1$ .

Use the operator  $h(m)$  to denote  $m$  lateral derivatives of the fluid thickness  $h$ ,  $\partial_x^m h$ , and similarly  $uuj(m)$  denotes  $m$  lateral derivatives of the layer mean velocity  $\bar{u}_j$ ,  $\partial_x^m \bar{u}_j$ . Use  $d$  to count the number of lateral  $x$  derivatives so we can easily truncate the asymptotic expansion. These operators depend upon time and lateral space. Then the spatial derivative  $\partial_x h(m) = h(m+1)$ , and the time derivative  $\partial_t h(m) = \partial_x^m gh$ , for example.

```

1  % Computer algebra derives two layer model of thin fluid film.
2  % MC and AJR, 5 May 2014
3  on div; off allfac; on revpri; linelength 70$
4  factor gam,d,small,re,nu,gx,gy;
5  operator h; operator uu1; operator uu2;
6  hx:=h(1)*d;
7  depend h,xx,tt;
8  depend uu1,xx,tt;
9  depend uu2,xx,tt;
10 let { df(h,xx)=>h(1), df(h(~m),xx)=>h(m+1)
11      , df(h,tt)=>gh , df(h(~m),tt)=>df(gh,xx,m)
12      , df(uu1,xx)=>uu1(1), df(uu1(~m),xx)=>uu1(m+1)
13      , df(uu1,tt)=>gu1 , df(uu1(~m),tt)=>df(gu1,xx,m)
14      , df(uu2,xx)=>uu2(1), df(uu2(~m),xx)=>uu2(m+1)
15      , df(uu2,tt)=>gu2 , df(uu2(~m),tt)=>df(gu2,xx,m)
16      };
17 % coordinate transfer;
18 depend xx,x,z,t;
19 depend zz,x,z,t;
20 depend tt,x,z,t;
21 let { df(~a,x)=>df(a,xx)*d-zz*hx/h*df(a,zz)
22      , df(~a,t)=>df(a,tt)-zz*gh/h*df(a,zz)
23      , df(~a,z)=>df(a,zz)/h
24      };
25 % operators for updating;
26 operator uinv; linear uinv;
27 let { uinv(1,zz,1)=>-zz^2/2+zz/6
28      , uinv(1,zz,2)=>-zz^2/2+1/8+2/3*(zz-1/2)
29      , uinv(zz^~p,zz,1)=>(-zz^(p+2)+zz/(p+3)/2^p)/(p+1)/(p+2)
30      , uinv(zz^~p,zz,2)=>(-zz^(p+2)+1/2^(p+2)
31      + (zz-1/2)*(8-(p+4)/2^p)/(p+3) )/(p+1)/(p+2)
32      };
33 operator mean; linear mean;
34 let { mean(1,zz,~a)=>1
35      , mean(zz^~p,zz,1)=>1/(p+1)/2^p
36      , mean(zz^~p,zz,2)=>(2-1/2^p)/(p+1)
37      };
38 operator wsolv; linear wsolv;

```

```

39 let { wsolv(zz^~n,zz,1)=>zz^(n+1)/(n+1)
40       , wsolv(1,zz,1)=>zz
41       , wsolv(zz^~n,zz,2)=>(zz^(n+1)-1/2^(n+1))/(n+1)
42       , wsolv(1,zz,2)=>zz-1/2
43     };
44 operator psolv; linear psolv;
45 let { psolv(zz^~n,zz,2)=>(1-zz^(n+1))/(n+1)
46       , psolv(1,zz,2)=>(1-zz)
47       , psolv(zz^~n,zz,1)=>(1/2^(n+1)-zz^(n+1))/(n+1)
48       , psolv(1,zz,1)=>(1/2-zz)
49     };
50 % linear initial approximation;
51 % use small to count the number of U_j factors;
52 u1:=small*uu1*zz*4;
53 u2:=small*(uu1*(6-8*zz)+uu2*(4*zz-2));
54 p1:=small*h*(1-zz);
55 p2:=small*h*(1-zz);
56 w1:=w2:=gh:=gu1:=gu2:=0;
57 % truncate the asymptotic expansion;
58 d:=small;
59 grz:=1;
60 grx:=d*gx;
61 let {small^3=>0, gam^7=>0};
62 for it:=1:99 do begin
63   ok:=1;
64   % update w with continuity and no flow through bed;
65   resc1:=df(u1,x)+df(w1,z);
66   w1:=w1+(w1d:=-h*wsolv(resc1,zz,1));
67   resc2:=df(u2,x)+df(w2,z);
68   w2:=w2-h*wsolv(resc2,zz,2)+sub(zz=1/2,w1d);
69   bcw1:=sub(zz=0,w1);
70   bcw2:=sub(zz=1/2,w2-w1);
71   write clengths:={length(resc1),length(resc1)
72                   ,length(bcw1),length(bcw2)};
73   ok:=if {resc1,resc2,bcw1,bcw2}={0,0,0,0} then ok else 0;
74   % update p from vertical momentum and surface normal stress;
75   resw2:=re*( df(w2,t)+u2*df(w2,x)+w2*df(w2,z) )
76           +df(p2,z) +grz -nu*(df(w2,x,2)+df(w2,z,2));
77   resw1:=re*( df(w1,t)+u1*df(w1,x)+w1*df(w1,z) )
78           +df(p1,z) +grz -nu*(df(w1,x,2)+df(w1,z,2));
79   restn2:= sub(zz=1,-p2*(1+hx^2) +2*nu*(df(w2,z)
80           +hx^2*df(u2,x)-hx*(df(u2,z)+df(w2,x))) );
81   p2:=p2+(p2d:=h*psolv(resw2,zz,2)+restn2);
82   p1:=p1+h*psolv(resw1,zz,1)+sub(zz=1/2,p2d);
83   bcp1:=sub(zz=1/2,p1-p2);

```



```

84 write wlengths:={length(resw2),length(resw1)
85                 ,length(restn2),length(bcp1)};
86 ok:=if {resw1,resw2,restn2,bcp1}={0,0,0,0} then ok else 0;
87 % update u from horizontal momentum,
88 % bed and surface tangential stress
89 resu1:=-re*( df(u1,t)+u1*df(u1,x)+w1*df(u1,z) )
90           -df(p1,x) +grx +nu*(df(u1,x,2)+df(u1,z,2));
91 resu2:=-re*( df(u2,t)+u2*df(u2,x)+w2*df(u2,z) )
92           -df(p2,x) +grx +nu*(df(u2,x,2)+df(u2,z,2));
93 bctt:=-sub(zz=1, (1-hx^2)*(df(u2,z)+df(w2,x))
94         +2*hx*(df(w2,z)-df(u2,x)) )
95       +(1-gam)*(sub(zz=1,u2)-sub(zz=1/2,u2))*2/h;
96 bcbed:=sub(zz=0,u1);
97 ccc:=-sub(zz=1/2,u1)+sub(zz=1/2,u2);
98 cc1:=- (1-gam/2)*sub(zz=1/2,df(u1,z))
99       +(gam/2)*sub(zz=1/2,df(u2,z))
100      +(1-gam)*sub(zz=1/2,u1)*2/h;
101 write ulengths:={length(resu1),length(resu2),length(bctt)
102                 ,length(bcbed),length(cc1),length(ccc)};
103 ok:=if {resu1,resu2,bctt,bcbed,cc1,ccc}={0,0,0,0,0,0}
104       then ok else 0;
105 % update the evolution and the lateral velocity;
106 gu1:=gu1+(gd1:=3*nu*cc1/h
107           +mean(3*zz*resu1,zz,1))/re/small;
108 gu2:=gu2+(gd2:=3/2*nu*cc1/h+3*nu*bctt/h
109           +mean(3*zz/2*resu1,zz,1)
110           +mean(3*(zz-1/2)*resu2,zz,2))/re/small;
111 u1:=u1+(u1d:=uinv(resu1-gd1*zz*4,zz,1)*h^2/nu);
112 u2:=u2+uinv(resu2-gd1*(6-8*zz)-gd2*(4*zz-2),zz,2)*h^2/nu
113       +sub(zz=1/2,u1d)*(3-4*zz);
114 % update the free surface evolution;
115 gh:=sub(zz=1,w2-u2*hx);
116 showtime;
117 if ok then write it:=it+100000;
118 end;
119 % check correct amplitudes for the lateral shear momentum
120 amp1:=-u1*small+mean(u1,zz,1);
121 amp2:=-u2*small+mean(u2,zz,2);
122 % Now stabilise high wavenumber modes
123 lgu1:=gu1-a*df(h^2*df(gu1*small,x),x)/small;
124 lgu2:=gu2-a*df(h^2*df(gu2*small,x),x)/small$
125 % write out the leading equation;
126 dhdt:=gh;
127 on rounded; print_precision 4;
128 lreuidt:=re*lgu1;

```

```

129 lredu2dt:=re*lggu2;
130 end;
131 % derive the slow manifold of the two-layer model
132 operator uu;
133 depend uu,xx,tt;
134 let { df(uu,xx)=>uu(1), df(uu(~m),xx)=>uu(m+1)
135 , df(uu,tt)=>gu , df(uu(~m),tt)=>df(gu,xx,m)
136 };
137 let { uu1(~p)=>df(uu1,xx,p)
138 , uu2(~p)=>df(uu2,xx,p)
139 };
140 % initial approximation of the two layer velocities
141 uu1:=uu*2/3;
142 uu2:=uu*4/3;
143 gu:=0;
144 let gamd^7=>0;
145 fac:=9/2;
146 for it:=1:19 do begin
147 res1:=-df(uu1,t)+gu1+(1-gamd)*fac*nu/re/h^2*(-4*uu1+2*uu2);
148 res2:=-df(uu2,t)+gu2+(1-gamd)*fac*nu/re/h^2*(+2*uu1-1*uu2);
149 write ulengths:=map(length(~a),{res1,res2});
150 gu:=gu+(gud:=(res1+2*res2)*3/10);
151 uu1:=uu1+h^2*re/nu/6/fac*(res1-gud*2/3);
152 uu2:=uu2+h^2*re/nu/3/fac*(res2-gud*4/3);
153 if {res1,res2}={0,0} then write it:=it+10000;
154 end;
155 % check the average
156 resamp:=(uu1+uu2)/2-uu;
157 % write out results
158 fullprob:={gamd=>1,small=>1};
159 on rounded; print_precision 4$
160 dhdt:=sub(fullprob,gh);
161 redudt:=sub(fullprob,re*gu);
162 off rounded;
163 end;

```